

Anomalous Diffusion of Superparamagnetic Walkers with Tailored Statistics

Alessia Gentili¹, Rainer Klages^{2,3}, Giorgio Volpe^{1*}

¹Department of Chemistry, University College London, 20 Gordon Street, London WC1H 0AJ, United Kingdom.

²Centre for Complex Systems, School of Mathematical Sciences, Queen Mary University of London, Mile End Road, London E1 4NS, United Kingdom.

³London Mathematical Laboratory, 8 Margravine Gardens, London W6 8RH, United Kingdom.

*Corresponding author(s). E-mail(s): g.volpe@ucl.ac.uk;

Abstract

From life sciences and ecology to quantum physics and finance, anomalous diffusion appears in countless complex systems as a signature of emergent transport properties beyond Brownian motion.¹⁻⁹ Despite substantial theoretical progress,¹⁰⁻¹⁶ the experimental study of real-world systems exhibiting anomalous diffusion remains challenging due to an intrinsically elusive ground truth and the limited information contained in typical single trajectories.¹⁶ Here, unlike previous experimental systems,^{8,17-22} we demonstrate the controlled generation of two-dimensional trajectories with fully tailored statistics spanning the entire spectrum of anomalous diffusion, from subdiffusion to superdiffusion, and over statistically significant temporal and spatial scales (covering at least two decades). We achieve this feat by simultaneously tuning the step-length distribution and, critically, the velocity autocorrelation function of microscopic superparamagnetic colloidal walkers with magnetic fields during extended acquisitions. Supported by theoretical reasoning, fine control of these two quantities combined allows us to generate trajectories compatible with Lévy walks and fractional Brownian motion with tailored anomalous diffusion exponents. We envisage that our approach will offer a robust, controllable experimental framework for validating and advancing theoretical models, analysis techniques, and predictive tools to study anomalous diffusion in real-life phenomena. These include transport in physical and biological systems,^{5,7,8,23} animal movement,^{4,24} human ecology,^{25,26} and financial markets.^{9,27,28}

Anomalous diffusion encompasses all diffusion phenomena characterized by a non-linear power-law scaling of the mean square displacement in time ($\text{MSD}(t) \sim t^\mu$), where μ is the anomalous diffusion exponent, including superdiffusion ($\mu > 1$) and subdiffusion ($\mu < 1$).^{1,3,6,9-16} Deviations from Brownian motion ($\mu = 1$) leading to anomalous diffusion are found in the transport properties of many complex real-life systems.^{1-9,16-33} Signatures compatible with fundamental theoretical models (e.g., Lévy walks⁶ and fractional Brownian motion¹³) have emerged in fields as disparate as quantum physics,⁸ cell biology,^{29,30} material science,³¹ animal foraging,⁴ human ecology,^{25,26} and climate^{32,33} and financial^{27,28} records. Often, these systems also constitute the primary sources of experimental data on the topic.

Characterized by non-Gaussian⁶ and non-Markovian¹² behavior, studying anomalous diffusion directly from the measurement of individual trajectories in these complex real-life systems is challenging. This is because the experimental ground truth is typically unknown and the statistical information available in real-life trajectories (often short and noisy) is a prohibitively limiting factor.^{16,34} At the same time, experimental systems capable of reliably generating extended trajectories of known ground truth and with tailored statistics across the whole range of anomalous diffusion remain elusive. This significantly constrains our ability to investigate anomalous diffusion experimentally under controlled conditions. Current attempts, which include microscopic systems (e.g., cold atoms,⁸ lipid membranes,²¹ colloids,¹⁹ droplets²⁰ and optical vortices²²) as well as macroscopic optical materials¹⁷ and robots,¹⁸ have only demonstrated one value of the anomalous diffusion exponent μ (other than $\mu = 1$)^{17,19,20} or, at best, a few within a single system-specific regime of anomalous diffusion (either subdiffusion or superdiffusion).^{8,18,21,22} Often, the trajectories are also short, thus providing limited statistics in space and time (below one decade).^{8,19,20} Advances in the experimental study of anomalous diffusion have therefore relied heavily on simulations and, recently, machine learning tools to enhance data analysis.^{16,35}

In Fig. 1, we demonstrate the possibility of generating two-dimensional experimental trajectories exhibiting anomalous diffusion over statistically significant temporal and spatial scales (covering at least two decades) by controlling the motion of individual superparamagnetic colloidal walkers of diameter $13.8 \pm 0.4 \mu\text{m}$ in external rotating magnetic fields (Methods). By simultaneously tuning the colloidal walkers' step-length distribution and, importantly, their velocity autocorrelation function, we reproduce fundamental anomalous diffusion patterns with fully tailored statistics spanning the entire spectrum of anomalous diffusion, from subdiffusion to superdiffusion. These patterns are compatible with models of Lévy walks (Figs. 2 and 3) and fractional Brownian motion (Fig. 4). We use two concentric Halbach cylinders,³⁶ a dipole and a quadrupole, to generate a constant magnetic field gradient $|\nabla|\mathbf{B}|| \sim 0.9 \text{ T m}^{-1}$ (Figs. 1a and S1, Table 1, Methods). This gradient translates into a constant magnetic force $\mathbf{F}_B = |\mathbf{m}|\nabla|\mathbf{B}|$, where \mathbf{m} is the particles' magnetic moment, that drives the walkers at constant speed in its direction, $v_c = |\mathbf{v}| = \frac{\mathbf{F}_B}{6\pi\eta R}$ (Methods), where \mathbf{v} is the particle's velocity, R its radius, and η the fluid's viscosity.³⁷ By rotating the quadrupole around the fixed dipole at discrete times t_n with n an integer (Fig. 1a, Methods), we can reorient \mathbf{F}_B and, hence, the particle's motion direction to generate extended tailored trajectories in a two-dimensional comoving frame (Fig. 1b). This is a coordinate

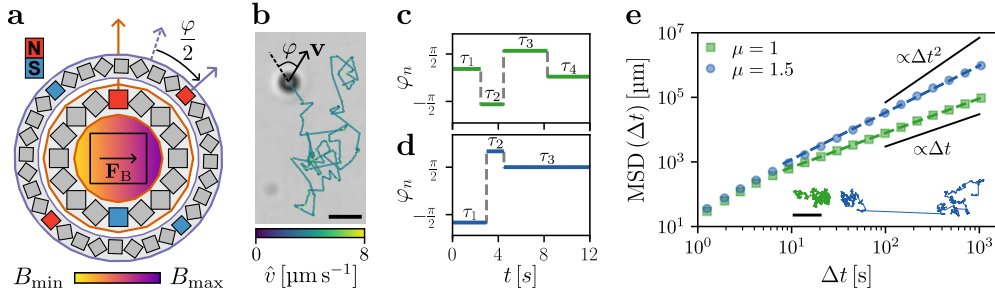


Fig. 1 Anomalous diffusion of superparamagnetic colloidal walkers in the comoving frame. (a) Two concentric Halbach cylinders (inner dipole; outer quadrupole) generate a linear magnetic field \mathbf{B} (color gradient) and a constant force \mathbf{F}_B (black arrow) on a sample (black rectangle) of dilute superparamagnetic colloids at their center. The gray squares in the cylinders denote individual cubic magnets with the cylinders' magnetic north (red) and south (blue) shown. Rotating the quadrupole (purple arrows) around the fixed dipole (orange arrow) reorients \mathbf{F}_B and the particles' motion direction. Two consecutive rotations define the particle's turning angle φ as twice the quadrupole rotation angle (Methods). (b) Example trajectory (color-coded for its instantaneous speed \hat{v}) of a superparamagnetic silica sphere of diameter $13.8 \pm 0.4 \mu\text{m}$ moving at approximately constant speed (\hat{v}) = $4.6 \pm 0.8 \mu\text{m s}^{-1}$. This motion can be described in a comoving frame by rotations of the particle's velocity vector \mathbf{v} with φ . Scale bar: $25 \mu\text{m}$. (c-d) Example bespoke sequences φ_n in time t of uniformly distributed $\varphi \in [-\pi, \pi)$ obtained by sampling the quadrupole rotation time τ_n (solid lines) from (c) a half-Gaussian and (d) a power-law (anomalous exponent $\mu = 1.5$) distribution. (e) Time-averaged mean squared displacements (MSD, symbols) and corresponding trajectories (inset) yielding normal diffusion ($\mu = 1$, green squares) or superdiffusion ($\mu = 1.5$, blue circles) at long times as confirmed by fitting the MSD logarithmic slope to a line (dashed lines). Diffusive ($\propto \Delta t$) and ballistic ($\propto \Delta t^2$) slopes shown for reference. Scale bar: 1 mm .

frame that defines the particle's motion in terms of its speed $|\mathbf{v}| \geq 0$ and turning angle $\varphi \in [-\pi, \pi)$, where here only the latter changes at times t_n (Figs. 1c-d, SI). Originally introduced by Ross and Pearson about a century ago,^{38,39} this coordinate frame has been used to analyze and model foraging organisms in movement ecology^{40,41} and to formulate advanced stochastic processes such as two-dimensional Lévy walks.^{42,43} Generating stochastic dynamics in a comoving frame implies a fundamental change of perspective compared to defining stochastic processes in a more standard fixed Cartesian frame (SI). Assuming overdamped dynamics, two decoupled time-discrete stochastic equations allow us to formulate our particle's two-dimensional motion in the comoving frame as (SI)⁴¹

$$\varphi_n = \xi_{\varphi,n} \quad (1)$$

$$v_n = \xi_{v,n} \quad (2)$$

where $\xi_{\varphi,n}$ and $\xi_{v,n}$ represent arbitrarily complex noise terms driving each coordinate's dynamics sampled at (non-necessarily equally spaced) discrete times $t_n = t_{n-1} + \tau_n$ with τ_n the quadrupole rotation time (Methods, Fig. 1). Given constant speed, the particle runs a distance $\ell_n = v_c \tau_n$ ballistically during flight time τ_n . If we sample τ_n

from an arbitrary noise distribution $\xi_{\tau,n}$, we can replace Eq. 2 with (SI)

$$\ell_n = v_c \xi_{\tau,n} \quad (3)$$

where the step length and flight time distributions are related by $\xi_{\ell,n} = v_c \xi_{\tau,n}$.

By defining appropriate distributions for $\xi_{\varphi,n}$ (through the quadrupole rotation angle) and $\xi_{\tau,n}$ (through the quadrupole rotation time) and by sampling independent and identically distributed random variables from these distributions in time, random walks with different statistical properties can be generated in the comoving frame experimentally under the constraint of constant speed (Fig. 1, Methods, SI). For example, sampling $\xi_{\varphi,n}$ from the uniform distribution on the circle, we can generate particle trajectories yielding long-time normal diffusion or superdiffusion (Fig. 1e) when $\xi_{\tau,n}$ is sampled from either a half-Gaussian distribution⁴⁴ (Fig. 1c) or a power law distribution with exponent $\alpha = 3 - \mu$ as in Lévy walks⁴² (Fig. 1d for $\alpha = \mu = 1.5$) (Methods, SI). Unlike the normal diffusion case, the superdiffusive trajectory shows some occasional long jumps displaying the spatial features typical of Lévy walks. The random nature of these long jumps is confirmed by the mean displacement of the particle in time being nearly zero ($< 0.07R$, with R the particle's radius). The narrow distributions of the instantaneous particle's speed \hat{v} for each trajectory confirm that our particles move at an approximately constant speed (Fig. S2), validating the use of Eqs. 1 and 3 to formulate their motion. A long-time fit of the time-averaged mean squared displacement (MSD) calculated from each trajectory (for $\Delta t > 8$ s, i.e. above the short-time persistence of the trajectory due to the magnetic drive)⁴⁵ confirms the two desired diffusion regimes over two decades (Fig. 1e, Methods). From the fits, we indeed estimate the anomalous diffusion exponents to be $\hat{\mu} = 1.0653 \pm 0.0002$ and $\hat{\mu} = 1.5473 \pm 0.0004$, respectively.

A deeper analysis of the experimental trajectories' statistics, based on their segmentation with the detected turning points (Fig. S3, Methods), further confirms that the final particles' dynamics we generate are consistent with the desired diffusion regimes (Fig. 2). Beyond the mean squared displacements (Fig. 1e), we can extract the flight times $\hat{\tau}_n$, the step lengths $\hat{\ell}_n$ and the turning angles $\hat{\varphi}_n$ of the particle directly from each trajectory (Methods). The step lengths ℓ_n depend linearly on the respective flight times $\hat{\tau}_n$ (Fig. S4), thus providing an independent confirmation of the particles' approximately constant speed. The probability distribution functions (PDFs) of $\hat{\varphi}_n$, $\hat{\tau}_n$ and $\hat{\ell}_n$ (Figs. 2a-b and S5) confirm that we are reproducing the desired distributions as defined by the quadrupole's rotation angle and time (Methods): for both trajectories in Fig. 1e, the distribution of the turning angle is uniform on the circle (Fig. S5a-b), thus matching the intended sampling specified by the quadrupole's rotation in line with Eq. 1 (i.e., $\text{PDF}(\hat{\varphi}_n) \sim \text{PDF}(\varphi_n)$, SI); both distributions of $\hat{\ell}_n$ and $\hat{\tau}_n$ show exponential and power-law scaling (with $\hat{\mu} \approx 1.5$ over two decades, Table 2), respectively consistent with normal diffusion ($\mu = 1$) and superdiffusion for $\mu = 1.5$ (Figs. 2a-b and S5c),⁴² thus matching the intended sampling specified by the quadrupole's rotation times in line with Eq. 3 (i.e., $\text{PDF}(\hat{\ell}_n) \sim \text{PDF}(\langle \hat{v} \rangle \hat{\tau}_n) \sim \text{PDF}(\langle \hat{v} \rangle \tau_n)$, SI). The time-averaged experimental velocity auto-correlation function $C_v(\Delta t)$ at lag times Δt

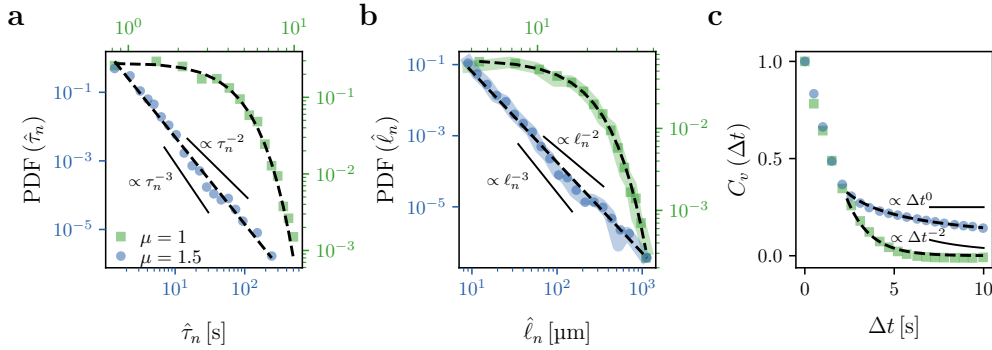


Fig. 2 Tailored diffusion statistics of superparamagnetic colloids. (a-b) Probability distribution functions (PDF) of (a) flight times $\hat{\tau}_n$ between turns and (b) step lengths $\hat{\ell}_n$ extracted from trajectories for the cases of normal diffusion ($\mu = 1$, green squares) and superdiffusion ($\mu = 1.5$, blue circles) as in Fig. 1e. (c) Respective normalized time-averaged velocity autocorrelation C_v as a function of lag time Δt . In a-c, fitting curves to the functions (dashed lines) show exponential and power-law scaling respectively consistent with normal diffusion ($\mu = 1$) and superdiffusion ($\mu = 1.5$, Table 2). The thick background lines in b represent $\text{PDF}(\langle v \rangle \hat{\tau}_n)$, showing that $\text{PDF}(\hat{\ell}_n) \sim \text{PDF}(\langle v \rangle \hat{\tau}_n)$ with $\langle v \rangle$ the particle's measured mean instantaneous speed (Fig. S2). The axis colors in a-b reflect those of the respective distributions. Diffusive (a: $\propto \tau_n^{-3}$; b: $\propto \ell_n^{-3}$; c: $\propto \Delta t^{-2}$) and ballistic (a: $\propto \tau_n^{-2}$; b: $\propto \ell_n^{-2}$; c: $\propto \Delta t^0$) limits shown for reference.

is also in agreement with theoretical expectations for the two regimes (Fig. 2c, Methods).^{1,46} The tail of this function decays as an exponential for the diffusive case due to the short-term persistence in the magnetic field⁴⁶ and, asymptotically, as a power-law ($\sim \Delta t^{\hat{\mu}-2}$ with $\hat{\mu} = 1.434 \pm 0.005$, Table 2) for the superdiffusive case, as expected for unbiased Lévy walks.⁶

The statistics in Figs. 1 and 2 demonstrate the proof-of-concept generation of trajectories yielding superdiffusion consistent with a Lévy walk model over two decades in space and time. For our approach to be truly transformative, control over the anomalous diffusion exponent μ is desirable. Fig. 3 shows the possibility of tuning the values of μ between the diffusive ($\mu = 1$) and ballistic ($\mu = 2$) limits by controlling the distributions of the step lengths ℓ_n . By sampling φ_n from the uniform distribution on the circle and τ_n from power-law distributions of varying exponent $\alpha = 3 - \mu$ (Fig. S6),⁴² we can generate trajectories in the comoving frame according to Eqs. 1 and 3 yielding different regimes of superdiffusion in a controllable way under the experimental constraint of constant speed (Table 2). Fig. 3a (inset) shows example trajectories for different values of μ : as the anomalous diffusion exponent increases, the particles tend to move ballistically over longer distances before a random change in orientation occurs. As expected for unbiased Lévy walks,⁶ the mean value of the displacements for each trajectory is near zero ($< 0.07 R$). Importantly, the four independent measurements $\hat{\mu}$ of the anomalous diffusion exponent obtained from fitting mean squared displacements (Fig. 3a, $\sim \Delta t^{\hat{\mu}}$), probability distribution functions of flight times $\hat{\tau}_n$ (Fig. S6, $\sim \hat{\tau}_n^{\hat{\mu}-4}$), probability distribution functions of step lengths $\hat{\ell}_n$ (Fig. 3b-e,

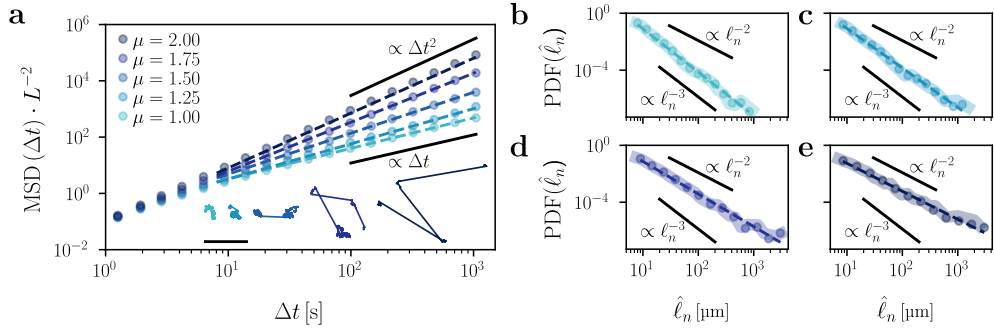


Fig. 3 Tailoring superdiffusion by controlling step-length distributions. (a) Normalized time-averaged mean squared displacements (MSD, dots) yielding superdiffusion at long times for trajectories (inset) generated according to Eqs. 1 and 3 by sampling the turning angle φ_n from the uniform distribution on the circle and the flight time τ_n from power-law distributions of varying exponent $\alpha = 3 - \mu$ between the normal diffusive ($\mu = 1$) and ballistic ($\mu = 2$) limits. Case for $\mu = 1.5$ as in Fig. 1e. Fit lines (dashed lines) confirm the different superdiffusive regimes (Table 2). The MSDs are normalized to the square of each particle's short-term persistence length L in the driving magnetic field. Scale bar: 5 mm. (b-e) Probability distribution functions (PDF, dots) of experimental step lengths $\hat{\ell}_n$ for (b) $\mu = 1$, (c) $\mu = 1.25$, (d) $\mu = 1.75$ and (e) $\mu = 2$. $\text{PDF}(\hat{\ell}_n) \sim \text{PDF}(\langle \hat{v} \rangle \hat{\tau}_n)$ (thick background lines). Case for $\mu = 1.5$ in Fig. 2b. Fit lines (dashed lines) show power-law scalings ($\sim \hat{\ell}_n^{\mu-4}$) consistent with the desired ground-truth values of μ (Table 2). Diffusive (a: $\propto \Delta t$; b-e: $\propto \hat{\ell}_n^{-3}$) and ballistic (a: $\propto \Delta t^2$; b-e: $\propto \hat{\ell}_n^{-2}$) limits shown for reference.

$\sim \hat{\ell}_n^{\mu-4}$) and velocity autocorrelation functions (Fig. S7, $\sim \Delta t^{\mu-2}$) all scale in agreement with theoretical expectations for Lévy walks at the respective ground-truth value of μ (Table 2).⁶

Beyond controlling the distributions of (independent and identically distributed) step lengths, a second paradigmatic class of anomalous diffusion dynamics emerges when the particle's displacements are not independent but correlated in time instead.¹² A famous example for this type of dynamics is fractional Brownian motion where the driving noise is no longer white but colored.^{13,47} This stochastic process can generate the whole spectrum of anomalous diffusion under parameter variation, from subdiffusion ($\mu < 1$) to superdiffusion ($\mu > 1$) through normal diffusion ($\mu = 1$).^{13,47} Experimentally, we implemented Eqs. 1 and 3 by pregenerating sequences of flight times τ_n and turning angles φ_n that yield an analogue of two-dimensional fractional Brownian motion in the comoving frame under the constraint of constant speed (Methods, SI). In analogy to the transformation between Lévy flights and walks, we refer to this constant-speed process as *fractional Brownian walks*. Fig. 4 shows that, as μ increases, the corresponding trajectories (Fig. 4a, inset) become less localized and more ballistic. The particles' tendency to turn backward (negative persistence) reduces in favor of its forward propagation (positive persistence) (polar plots, Fig. S8). A long-time fit of the time-averaged mean squared displacements (MSDs) calculated from each trajectory (Fig. 4a, Table 3) confirms the shift from subdiffusion (sublinear MSD, $\mu < 1$) to superdiffusion (superlinear MSD, $\mu > 1$) through normal diffusion (linear MSD, $\mu = 1$), when the particles' velocities show a transition from negative to positive correlations (Fig. 4b, Table 3) in agreement with theoretical expectations (Methods,

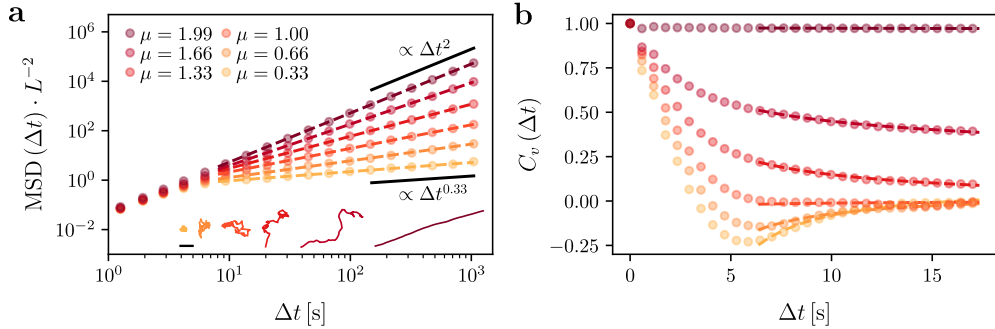


Fig. 4 Tailoring anomalous diffusion by controlling the velocity autocorrelation function. (a) Normalised time-averaged mean squared displacements (MSD, dots) yielding different anomalous diffusion regimes at long times, from subdiffusion ($\mu < 1$) to superdiffusion ($\mu > 1$) through normal diffusion ($\mu = 1$), for trajectories (inset) consistent with fractional Brownian motion (Methods, SI). Fit lines (dashed lines) confirm the different anomalous diffusion regimes (Table 3). The MSDs are normalized to the square of each particle’s short-term persistence length L in the driving magnetic field. Diffusive ($\propto \Delta t$) and ballistic ($\propto \Delta t^2$) limits shown for reference. Scale bar: $100 \mu\text{m}$. (b) Respective normalized time-averaged velocity autocorrelation functions C_v (dots) as a function of lag time Δt calculated from the trajectories in **a** for different ground-truth values of μ . Fitting the tail of the data with a quadratic polynomial scaled by a power law (dashed lines) confirms the asymptotic scaling characteristic of fractional Brownian motion at different values of μ ($\sim \hat{\mu}(\hat{\mu} - 1)\Delta t^{\hat{\mu}-2}$, Table 3).

SI).^{48,49} Therefore, these two consistent independent measurements (i.e., by fitting the MSD and C_v) of the anomalous diffusion exponent associated with each trajectory strongly support the tailored generation of different types of anomalous diffusion dynamics, compatible with fractional Brownian motion, by the spatio-temporal control of the particle’s turning angles and flight times in the comoving frame (Table 3).

In conclusion, supported by theoretical reasoning, we have demonstrated finely tuned stochastic dynamics of colloidal particles in a comoving frame. By controlling just two experimental parameters (i.e., the particles’ turning angles and flight times), we have generated two-dimensional constant-speed trajectories with tailored anomalous diffusion statistics over statistically relevant time and spatial scales. These trajectories span the entire spectrum of anomalous diffusion, from subdiffusion to superdiffusion, and are characterized by different distributions and correlations of random variables. The dynamics we have generated are compatible with two-dimensional models of normal diffusion,³ Lévy walks,⁶ and fractional Brownian motion.¹³ While these higher-dimensional (non-Markovian) stochastic processes are often defined in a stationary Cartesian frame, our experimental approach requires their formulation in a comoving frame. The need for such formulation poses interesting theoretical questions about the relation between stochastic processes defined in both frames. Arguably, the comoving frame is the more natural one to study the (anomalous) dynamics of active agents,⁵⁰ such as organisms and robots, driven by an internal source of randomness generated by the agents themselves.^{41,43} Unlike natural processes^{1–7,9,16,23–33} and previous synthetic experimental systems,^{8,17–22} our experimental and theoretical

framework therefore paves the way for controllable experiments on anomalous diffusion, where the ground truth is known. We thus anticipate that our framework will empower researchers to deepen our understanding of anomalous diffusion and enhance our comprehension of real-world complex systems exhibiting it across various fields and scales, from the life sciences^{5,7} to macroscopic natural and human processes.^{4,24–28}

Supplementary information. This article is accompanied by a Supplementary Information file.

Acknowledgments. A.G and G.V. acknowledge sponsorship for this work by the US Office of Naval Research Global (award no. N62909-18-1-2170).

Declarations

Conflict of interest

The authors declare no competing interests.

Data availability

All data supporting the findings of this study are available in the manuscript and its Supplementary Information. Further data can be obtained from the corresponding author on reasonable request.

Code availability

Code in support of the finding of this study can be obtained from the corresponding author on reasonable request.

Author contributions

Author contributions are defined based on the CRediT (Contributor Roles Taxonomy) and listed alphabetically. Conceptualisation: G.V. Data curation: A.G. Formal analysis: A.G., R.K., G.V. Funding acquisition: G.V. Investigation: A.G. Methodology: A.G., R.K., G.V. Project administration: G.V. Resources: G.V. Software: A.G., G.V. Supervision: G.V. Validation: A.G., G.V. Visualisation: A.G. Writing – original draft: G.V. Writing – review and editing: All.

Methods

Materials

Glass microscopy slides (25 mm x 75 mm x 1 mm, Eppredia) and glass coverslips (24 mm x 24 mm x 0.14 mm) for sample preparation were purchased from Thermo Fisher and VWR, respectively. The following chemicals were purchased and used as received: acetone ($\geq 99.8\%$, Sigma-Aldrich), ethanol ($\geq 99.8\%$, Fisher Scientific), ethylene glycol (Sigma-Aldrich), Tween 20 (Sigma-Aldrich). Deionised (DI) water ($\geq 18\text{ M}\Omega\text{ cm}$,

type II Water) was collected from a Milli-Q purification system. Aqueous colloidal dispersions (5% w/v) of superparamagnetic silica (SiO_2) particles were purchased from Microparticles GmbH. Parafilm (Bemis Parafilm M Laboratory Wrapping Film), used as spacer for the sample chamber, was purchased from Fisher Scientific. Two-part epoxy glue (Gorilla Epoxy) for sealing the samples was purchased from RS Components. The neodymium magnets used to build the Halbach cylinders were purchased from K&J Magnetics, Inc. (B666-N52) and supermagnete (W-07-N). PA 2200 (nylon powder) was used to 3D-print the encasing of the magnets for the cylinders.

Colloidal Dispersion

We used superparamagnetic silica (SiO_2) colloidal particles with a diameter of $13.8 \pm 0.4 \mu\text{m}$, an iron oxide content greater than 5 wt. %, and a high density of approximately 1.5 g cm^{-3} , as estimated by the manufacturer. Before each experiment, we gradually diluted the original batch dispersion in a 50% ethylene glycol and 50% DI water solution by volume to achieve very low particle concentrations ($< 10^{-5}$ w/v%) and avoid interparticle interactions and chain formation in a magnetic field. The viscosity of this solution is approximately four times that of pure DI water⁵¹ to reduce the particles' speed when exposed to the high magnetic fields generated by the Halbach cylinders (Fig. 1). Typical Péclet numbers range between 4000 and 6000. Such high values indicate that Brownian motion is negligible and directed motion dominates the dynamics of our particles.⁵⁰ To prevent the particles from sticking to the glass slides during experiments, we added small traces (< 0.002 v/v%) of a 10% Tween 20 aqueous solution to the final dispersion. By preventing sticking and by increasing viscosity to reduce occurrences of particles exiting the field of view, we were able to control their dynamics for up to 9 hours.

Sample Chamber

We confined 62 μL of the colloidal dispersion within a quasi-two-dimensional chamber assembled from a microscope slide (bottom layer, cut to approximately 25 mm x 28 mm x 1 mm) and a coverslip (top layer) using two strips of melted parafilm as spacers to obtain a thickness of $\approx 20 \mu\text{m}$. First, we cleaned both the glass slide and coverslip by sequentially immersing them in Coplin jars containing acetone, ethanol and DI water in an ultrasonic bath for 5, 10 and 15 minutes, respectively. Blowing the slide and coverslip dry with nitrogen gas removed excess water. We then placed two strips of parafilm (approximately 25 mm x 5 mm each) at opposite edges of the glass slide and let them melt on a hotplate at 60° , near the melting point of parafilm. Once the parafilm turned transparent (after about 3 minutes), we placed the coverslip on top, and applied slight pressure using the flat tip of a pair of tweezers to close the chamber. After cooling and loading the particles' dispersion, we sealed the chamber with two-part epoxy glue, and let it cure and rest for at least 20 minutes before each experiment.

Magnetic fields with Halbach cylinders

We generated the constant magnetic field gradient $\nabla|\mathbf{B}|$ needed to drive the colloidal walkers at constant speed $v_c = |\mathbf{v}|$ in the sample plane using two concentric Halbach cylinders (Figs. 1a and S1): an inner dipole (Fig. S1a) surrounded by an outer quadrupole (Fig. S1b).³⁶ These cylinders, constituted by circular arrays of permanent magnets (Fig. S1c), can produce controlled magnetic fields entirely within their core while canceling it on the outside. In our case, the axis of the cylinders is aligned along the direction (z in Fig. S1) perpendicular to the sample plane (xy in Fig. S1). The inner Halbach cylinder produces a strong homogeneous dipolar magnetic field \mathbf{B}^D in this plane with constant intensity B_0 along the y -axis (Fig. S1a,d-f), maximizing the magnetic moment \mathbf{m} of the superparamagnetic particles and aligning it along the field lines. The outer cylinder generates a weaker quadrupolar magnetic field \mathbf{B}^Q consisting of two orthogonal linear components in space (i.e., each with a constant derivative of magnitude G) (Fig. S1b,g-i). When the two arrays are coaxially aligned, the resulting field $\mathbf{B}(\mathbf{r})$ at position $\mathbf{r} = (x, y)$ is linear in space and given by³⁶

$$\mathbf{B}(\mathbf{r}) = \mathbf{B}^D(\mathbf{r}) + \mathbf{B}^Q(\mathbf{r}) = B_0 \begin{bmatrix} 0 \\ 1 \end{bmatrix} + G \begin{bmatrix} -\cos 2\beta & \sin 2\beta \\ \sin 2\beta & \cos 2\beta \end{bmatrix} \begin{bmatrix} x \\ y \end{bmatrix}, \quad (4)$$

where 2β is the angle of rotation of the magnetic field gradient induced by a β rotation of the quadrupole around the dipole. The direction of the gradient can therefore be adjusted by rotating the quadrupole with respect to the dipole (Fig. 1a), and the difference $\Delta\beta$ between two consecutive rotations of the quadrupole defines the particle's turning angle φ as $\varphi = 2\Delta\beta$ (Fig. 1a-b). As a result of combining a strong homogeneous dipolar magnetic field with a weaker constantly graded one, particles move in a well-defined, spatially independent and adjustable direction defined only by the component of the gradient parallel to \mathbf{B}^D (the y -component in Eq. 4).³⁷

We implemented a discrete version of the Halbach dipole with radius $r_c = 30.05$ mm using $k = 16$ cubic neodymium magnets (grade N52, remanence $B_R \sim 1.48$ T, relative permeability $\mu_R = 1.05$, side length $a_m = 9.5$ mm) with B_0 given by³⁶

$$B_0 = B_R \ln \left(\frac{r_{\text{out}}}{r_{\text{in}}} \right) \frac{1}{\sqrt{\mu_R}} \frac{\sin(2\pi/k)}{2\pi/k} \frac{k a_m}{\pi(r_{\text{out}}^2 - r_{\text{in}}^2)} \frac{h(6r_c^2 + h^2)}{(4r_c^2 + h^2)^{3/2}} \sim 85 \text{ mT} \quad (5)$$

where $r_{\text{in}} = 23.3$ mm and $r_{\text{out}} = 36.8$ mm are the cylinder's inner and outer radii, respectively (Fig. S1c), and $h = a_m$ its height. The cylinder radius r_c can be calculated from these two values as their average $r_c = (r_{\text{in}} + r_{\text{out}})/2$ and was chosen to be more than double the entire sample's size to prevent edge effects due to field inhomogeneities nearer to the magnets. Moreover, we implemented the Halbach dipolar cylinder with a vertical stack of two identical circular arrays separated by 15.3 mm,⁵² to reduce field inhomogeneity in the z -direction, thus minimizing any possible vertical magnetic drift of the colloids. Stacking the two arrays also produces an expected increase in field intensity by a factor of 1.351 with respect to the prediction in Eq. 5. We confirmed this increase with a Gaussmeter (Lake Shore Cryotronics, Inc., Model 420), measuring an average magnetic field of 111.38 ± 0.66 mT (Fig. S1d-f).

Similarly, we implemented a discrete version of the Halbach quadrupole with a larger radius $r_c = 46.7$ mm using $k = 32$ cubic neodymium magnets (grade N42, remanence $B_R \sim 1.32$ T, relative permeability $\mu_R = 1.05$, side length $a_m = 7$ mm) with G given by³⁶

$$G = \frac{2B_R}{\sqrt{\mu_R}} \left(\frac{1}{r_{\text{in}}} - \frac{1}{r_{\text{out}}} \right) \frac{\sin(3\pi/k)}{3\pi/k} \frac{k a_m^2}{\pi(r_{\text{out}}^2 - r_{\text{in}}^2)} \frac{h(h^4 + 10h^2r_c^2 + 30r_c^4)}{(4r_c^2 + h^2)^{5/2}} \sim 0.9 \text{ Tm}^{-1}. \quad (6)$$

This value was confirmed calculating the gradient ($0.98 \pm 0.08 \text{ Tm}^{-1}$) from the magnetic field intensities measured with the Gaussmeter (Fig. S1g-i).

Table 1 summarizes all parameters used to implement both Halbach cylinders. All magnets were held in place side by side by plastic molds (one for the dipole and one for the quadrupole), which we 3D-printed using Selective Laser Sintering (SLS) technology.

Experimental setup

We recorded particle's trajectories using a custom-built inverted microscope. The sample rested in the region of homogeneous dipolar field at the center of the Halbach dipole, which was supported by four metal pillars (Thorlabs). The sample holder was uncoupled from the dipole support to reduce transmission of vibrations due to the rotation of the quadrupole around the dipole. For the same reason, the quadrupole was mounted on a third separate support, vertically centered at the sample level, and connected to a high-speed motorized rotational stage (Laser2000, X-RSB060AD-KX13AG). To reorient the magnetic field gradient instantaneously with respect to the particle dynamics, we rotated the quadrupole at constant angular speed (60 rad s^{-1}). We chose this value because, during the time required by the quadrupole to complete the largest rotation in our experiments ($\Delta\beta = \pm\pi/2$), a particle traveled a distance comparable with our localization error on the determination of its centroid ($\approx 0.13 \mu\text{m}$), thus with negligible influence on the final trajectory. To reduce vibrations, we ramped the quadrupole rotation up to (down from) its maximum speed with a constant angular acceleration (deceleration) of 60 rad s^{-2} . For sample illumination, a monochromatic LED ($\lambda = 660 \text{ nm}$, Thorlabs, M660L4) equipped with an adjustable collimation adapter (Thorlabs, SM2F32-A) was mounted on this last support. To acquire long trajectories, we also uncoupled the imaging system from the part of the setup containing the sample. The imaging system was formed by two lenses projecting the image of the sample with a 4x magnification on a monochrome complementary metal-oxide-semiconductor (CMOS) camera (Thorlabs, DCC1545M). This system was mounted on a computer-controlled two-axis motorized translation stage (Thorlabs, PT1/M-Z8) to allow us to recenter the walker in the field of view of the camera ($1.3 \text{ mm} \times 1.6 \text{ mm}$), thus avoiding that the particle exited it in long linear stretches of its motion. Videos of particles were recorded with a frame rate of 11.94 frames per second (the inverse of the sampling time δt) using a custom MATLAB program that triggered the camera acquisition. The same program controlled the sequence of rotations of the quadrupole to implement bespoke patterns of anomalous

diffusion and the translation of the imaging system based on the particle’s position. During relatively long quadrupole rotation times (> 15 s), video recording was temporarily interrupted to automatically recenter the particle to the field of view every 2 seconds before recording was resumed. We translated the stage with a constant speed of 1 mm s^{-1} , approximately 200 times faster than typical particles’ speeds, i.e. almost instantaneously compared to the particles’ dynamics (Fig. S2). To reduce vibrations, we ramped the stage translation up to (down from) its maximum speed with a constant acceleration (deceleration) of 1 mm s^{-2} . Full particles’ trajectories were reconstructed by stitching together individual trajectories (Fig. S9, see *Trajectory stitching*) obtained from sequences of videos corresponding to each experiment using homemade Python scripts based on the `Trackpy` package.⁵³ Like this, we were able to acquire trajectories over centimeter-long scales over extended periods of time (up to 9 hours).

Trajectory stitching

We reconstructed full particles’ trajectories by stitching together individual trajectories from a sequence of N consecutive videos. To facilitate stitching, any two consecutive videos respectively finished and started with an at least 1-s long portion of the same step length ℓ_n in the trajectory (Fig. S9). These portions were reconnected by translating all the i points \mathbf{r}_i^{j+1} of the trajectory (with j and i both integers) defined in the coordinate system of the $(j+1)^{\text{th}}$ video back to the reference system of the j^{th} video (Fig. S9a). The origin of the coordinate system associated to each video is at the center of its field of view. As the particle is moving ballistically at the time of its recentering, we also accounted for the additional distance it travels between recordings (Fig. S9a). The translation between the reference systems of two consecutive videos is then given by

$$\mathbf{r}_i^j = \mathbf{r}_i^{j+1} + \mathbf{r}_M^j \approx (\mathbf{r}_i^{j+1} - \mathbf{r}_0^{j+1}) + \tau_\delta \langle \hat{v}_\ell \rangle \mathbf{u}_v + \mathbf{r}_M^j \quad (7)$$

where \mathbf{r}_i^j and \mathbf{r}_M^j are respectively the positions of \mathbf{r}_i^{j+1} and of the last recorded point of the j^{th} video in its reference system, and \mathbf{r}_0^{j+1} identifies the first particle’s position of the $(j+1)^{\text{th}}$ video in its reference system. If the particle is moving ballistically at approximately constant speed (as in our experiments, Fig. S2), the vector $\mathbf{r}_0^{j+1} \approx \tau_\delta \langle \hat{v}_\ell \rangle \mathbf{u}_v$, where τ_δ is the time elapsed between recordings, $\langle \hat{v}_\ell \rangle$ is the average particle’s speed in the two recorded portions of the step length being reconstructed, and $\mathbf{u}_v = (\cos(\theta), \sin(\theta))$ is the unitary vector in the current direction of motion, i.e. also defined by the same step length of the full trajectory which is being reconstructed. Finally, we linearly interpolated the displacement between the last point of the j^{th} video and the first point of the $(j+1)^{\text{th}}$ video by resampling with our experimental sampling time δt (the inverse of the frame rate). We repeated this procedure iteratively until the trajectory was fully reconstructed in the coordinate system of the first acquisition video. Fig. S9b-c verifies that any two reconnected portions in the reconstructed trajectory maintain the same direction of motion (Fig. S9b) and the validity of the relationship $\mathbf{r}_0^{j+1} \approx \tau_\delta \langle \hat{v}_\ell \rangle \mathbf{u}_v$ based on direct measurements of \mathbf{r}_0^{j+1} from image analysis and measurements of stage displacements (Fig. S9c), thus further confirming our constant speed approximation.

Distributions of quadrupole rotation times and turning angles

For trajectories yielding normal diffusion (Figs. 1 and 2, $\mu = 1$), we numerically generated sequences of N quadrupole rotation times τ_n drawn from a half-Gaussian distribution (Fig. S5). The probability density function (PDF) of this distribution is

$$\text{PDF}(\tau) = \frac{e^{-\tau^2/16}}{2\sqrt{\pi}}, \quad \tau \geq 0 \quad (8)$$

For trajectories yielding Lévy walks of exponent $\alpha = 3 - \mu$ (Figs. 1, 2 and 3), sequences of N quadrupole rotation times τ_n were numerically generated using the inverse method (Figs. S5 and S6):⁵⁴ by drawing r as a random number from a uniform distribution in $[0, 1)$, the variable $\tau = \tau_{\min}(1-r)^{-1/\alpha}$ follows a power-law distribution with exponent $(\alpha + 1)$ and lower bound τ_{\min}

$$\text{PDF}(\tau) = C\tau^{-(\alpha+1)}, \quad \tau \geq \tau_{\min} \quad (9)$$

where $C = \alpha\tau_{\min}^\alpha$ is a normalization constant. A power-law distribution with a lower bound was preferred over an α -stable Lévy distribution to optimize experimental time by focusing directly on the tail of the distributions. For this purpose, we set $\tau_{\min} = 1$ s to facilitate the detection of turning points in the trajectories (see *Turning point detection*).

Finally, we drew sequences of N turning angles φ_n from a uniform distribution over the half-open interval $[-\pi, \pi)$ for both normal diffusion and Lévy walks (Figs. S5 and S6). In all cases, we set N so that the cumulative sum of all τ_n was at least 3-hours long to observe anomalous diffusion in experiments over at least two decades in space and time.

For fractional Brownian motion, we generated sequences of (τ_n, φ_n) yielding a constant-speed analogue of this process in the comoving frame, which satisfies Eqs. 1 and 3, by adopting the protocol detailed in the Supplementary Information (SI). In analogy to the transformation between Lévy flights and walk, we refer to realizations of this process as *fractional Brownian walks*. Briefly, we transformed trajectories generated in simulations with a constant flight time $\tilde{\tau}_c$ and non-constant Gaussian-distributed velocities \tilde{v}_n in a Cartesian frame into trajectories of the same path topology with constant speed v_c and non-constant flight times τ_n in the comoving frame by doing the following (see details in SI): we first generated two-dimensional (time-discrete) Cartesian fractional Brownian motion from the Davies-Harte method⁵⁵ implemented in the Python package `stochastic` for all values of the anomalous exponent μ used in the experiments; in order to scale the average speed in simulations ($\tilde{v}_c = \langle \tilde{v}_n \rangle = \sqrt{\frac{\pi}{2}}\sigma_{\tilde{v}}$ for $\sigma_{\tilde{v}} = 1 \mu\text{m s}^{-1}$ and $\tilde{\tau}_c = 1$ s) to a representative a-priori estimate for the particle's experimental average speed $v_c = 4.5 \mu\text{m s}^{-1}$, we then used Eq. S33 with a scale factor of $\kappa = 3.6$ (defined by Eq. S23), thus effectively matching our experimental length scales; finally, we transformed the scaled sequences of speeds and turning angles (v_n, φ_n) associated to each trajectory into the corresponding (τ_n, φ_n) sequences for the rotation of the quadrupole implementing the transformation given by Eq. S29.

MSD calculation and fitting

For each trajectory, we calculated the time-averaged mean squared displacement (MSD) at discrete time lags $\Delta t = m\delta t$ (with δt the experimental sampling time and m an integer) as⁴⁵

$$\text{MSD}(\Delta t) = \frac{1}{T - \Delta t} \sum_{t=\delta t}^{T-\Delta t} \left[(x(t + \Delta t) - x(t))^2 + (y(t + \Delta t) - y(t))^2 \right] \quad (10)$$

where $\mathbf{r} = (x, y)$ are the trajectory's coordinates sampled at time steps $t = p\delta t$ (with p an integer), and $T = P\delta t$ (with $P = 12500$) is the total number of data points in the MSD calculations. We chose T to be shorter than the trajectory length, but large enough to extract anomalous diffusion exponents by fitting the MSD over at least two decades with strong statistical reliability. The scaling exponent $\hat{\mu}$ of the MSD was estimated with a linear fit in log-log scale in the asymptotic limit (i.e., for $\Delta t > 8$ s, after the short-time persistence transition point, Figs. 1c, 3a and 4a). The reported uncertainty associated with the estimated exponent $\hat{\mu}$ (Tables 2 and 3) corresponds to one standard deviation of the fit parameter.

Detection of turning points

We identified turning points along particles' trajectories based on the detection of local extrema in their velocity. Given that our particles move at nearly constant speed (Fig. S2), significant variations of this quantity should primarily reflect directional changes. Experimentally, we used variations of the absolute value of the acceleration magnitude gradient ($|\nabla|\mathbf{a}||$, Fig. S3a) as a noise-robust empirical proxy to identify these directional changes. To further minimize the impact of the experimental noise, this time series was preprocessed with a Savitzky-Golay filter with a 5-point kernel,⁵⁶ implemented with the Python `scipy.signal.savgol_filter` function. Prominent peaks were then identified using the Python `scipy.signal.find_peaks` function.⁵⁷ We validated this method for the independent detection of the turning points directly from the acquired trajectories by comparing their predicted values $\hat{\tau}_n$ against the ground truth from the sequences τ_n of quadrupole rotations (Fig. S3b). For all trajectories, we achieved a F_1 score of at least 0.83. Here, we computed the micro average of the F_1 score using the Python `sklearn.metrics.f1_score` function with a tolerance of five data points (~ 0.42 s),⁵⁸ i.e. we considered a predicted turning point a true positive if it was within five points of a ground truth value.

Experimental distributions of flight times and step lengths

After identifying the turning points along each trajectory, we calculated the probability density functions (PDFs) of the flight times $\hat{\tau}_n$ and step lengths $\hat{\ell}_n$ of the particles (Figs. 2, 3, S5, S6 and Fig. S10). For normal diffusion (Fig. 2a-b), the PDFs should decay exponentially in the long-time limit, which we verified by fitting them to a half-Gaussian function.^{3,6} For trajectories yielding Lévy walks (Figs. 2a-b and 3b-e), we verified their asymptotic power-law scaling and corresponding anomalous exponent

μ with a linear fit of the distribution tails on log-log scale (Table 2).^{3,6} To increase the tail statistics, we combined data from three different trajectories for each value of μ . For fractional Brownian walks, the PDFs should follow a Rayleigh distribution independent of the anomalous diffusion exponent μ (SI), as confirmed experimentally (Fig. S10).

Experimental velocity autocorrelation functions

For each trajectory, we calculated the normalized velocity autocorrelation function (VACF) as

$$C_v(\Delta t) = \frac{\langle \mathbf{v}(t) \cdot \mathbf{v}(t + \Delta t) \rangle}{\langle \mathbf{v}^2(t) \rangle} \quad (11)$$

where $\mathbf{v}(t)$ is the instantaneous particle's velocity at time t , Δt is the time lag for the calculation of the VACF and $\langle \dots \rangle$ indicates a time average. For normal diffusion, $C_v(\Delta t)$ follows an exponential decay as expected (Fig. 2c).^{6,46} For trajectories yielding Lévy walks, we confirmed that $C_v(\Delta t)$ decays as a power law of consistent anomalous exponent μ asymptotically (Fig. S7, Table 2).⁶ For fractional Brownian walks, we confirmed that $C_v(\Delta t)$ decays as the asymptotic functional form characteristic of this process given by $C_v(\Delta t) \simeq \frac{1}{2}\mu(\mu - 1)\Delta t^{\mu-2}$ for each value of μ (Fig. 4b, Table 3).⁵⁹

References

- [1] Bouchaud, J. & Georges, A. Anomalous diffusion in disordered media: Statistical mechanisms, models and physical applications. *Phys. Rep.* **195**, 127–293 (1990).
- [2] Metzler, R. & Klafter, J. The restaurant at the end of the random walk: Recent developments in the description of anomalous transport by fractional dynamics. *J. Phys. A: Math. Gen.* **37**, R161–R208 (2004).
- [3] Klages, R., Radons, G. & Sokolov, I. M. (eds.) *Anomalous transport: Foundations and Applications* (Wiley-VCH, Berlin, 2008).
- [4] Viswanathan, G., da Luz, M., Raposo, E. & Stanley, H. *The Physics of Foraging* (Cambridge University Press, Cambridge, 2011).
- [5] Höfling, F. & Franosch, T. Anomalous transport in the crowded world of biological cells. *Rep. Prog. Phys.* **76**, 046602 (2013).
- [6] Zaburdaev, V., Denisov, S. & Klafter, J. Lévy walks. *Rev. Mod. Phys.* **87**, 483–529 (2015).
- [7] Waigh, T. A. & Korabel, N. Heterogeneous anomalous transport in cellular and molecular biology. *Rep. Prog. Phys.* **86**, 126601 (2023).
- [8] Afek, G., Davidson, N., Kessler, D. A. & Barkai, E. Colloquium: Anomalous statistics of laser-cooled atoms in dissipative optical lattices. *Rev. Mod. Phys.* **95**, 031003 (2023).

- [9] Grebenkov, D., Metzler, R. & Oshanin, G. *Target search problems* (Springer, Berlin, 2025).
- [10] Podlubny, I. *Fractional differential equations* (Academic Press, New York, 1999).
- [11] Metzler, R. & Klafter, J. The random walk's guide to anomalous diffusion: A fractional dynamics approach. *Phys. Rep.* **339**, 1–77 (2000).
- [12] Coffey, W., Kalmykov, Y. P. & Waldron, J. T. *The Langevin Equation* (World Scientific, Singapore, 2004).
- [13] Biagini, F., Hu, Y., Øksendal, B. & Zhang, T. *Stochastic Calculus for Fractional Brownian Motion and Applications*. Probability and Its Applications (Springer, London, 2008).
- [14] Klafter, J. & Sokolov, I. *First Steps in Random Walks: From Tools to Applications* (Oxford University Press, Oxford, 2011).
- [15] Metzler, R., Jeon, J.-H., Cherstvy, A. G. & Barkai, E. Anomalous diffusion models and their properties: non-stationarity, non-ergodicity, and ageing at the centenary of single particle tracking. *Phys. Chem. Chem. Phys.* **16**, 24128–24164 (2014).
- [16] Muñoz-Gil, G. *et al.* Objective comparison of methods to decode anomalous diffusion. *Nat. Commun.* **12**, 6253 (2021).
- [17] Barthelemy, P., Bertolotti, J. & Wiersma, D. A Lévy flight for light. *Nature* **453**, 495–498 (2008).
- [18] Dimidov, C., Oriolo, G. & Trianni, V. Random walks in swarm robotics: an experiment with kilobots. In *International conference on swarm intelligence*, 185–196 (Springer, 2016).
- [19] Karani, H., Pradillo, G. E. & Vlahovska, P. M. Tuning the random walk of active colloids: From individual run-and-tumble to dynamic clustering. *Phys. Rev. Lett.* **123**, 208002 (2019).
- [20] Akella, V., Rajesh, R. & Panchagnula, M. V. Lévy walking droplets. *Phys. Rev. Fluids* **5**, 084002 (2020).
- [21] Coker, H. L. *et al.* Controlling anomalous diffusion in lipid membranes. *Biophys. J.* **116**, 1085–1094 (2019).
- [22] Gong, J., Li, Q., Zeng, S. & Wang, J. Non-gaussian anomalous diffusion of optical vortices. *Physical Review E* **109**, 024111 (2024).
- [23] Kanazawa, K., Sano, T. G., Cairoli, A. & Baule, A. Loopy lévy flights enhance tracer diffusion in active suspensions. *Nature* **120**, 364–367 (2020).

- [24] Vilk, O. *et al.* Unravelling the origins of anomalous diffusion: From molecules to migrating storks. *Phys. Rev. Res.* **4**, 033055 (2022).
- [25] Brockmann, D., Hufnagel, L. & Geisel, T. The scaling laws of human travel. *Nature* **439**, 462–465 (2006).
- [26] Gonzalez, M. C., Hidalgo, C. A. & Barabasi, A.-L. Understanding individual human mobility patterns. *Nature* **453**, 779–782 (2008).
- [27] Scalas, E., Gorenflo, R. & Mainardi, F. Fractional calculus and continuous-time finance. *Phys. A: Stat. Mech. Appl.* **284**, 376–384 (2000).
- [28] Plerou, V., Gopikrishnan, P., Amaral, L. A. N., Gabaix, X. & Stanley, H. E. Economic fluctuations and anomalous diffusion. *Phys. Rev. E* **62**, R3023 (2000).
- [29] Dieterich, P., Klages, R., Preuss, R. & Schwab, A. Anomalous dynamics of cell migration. *Proc. Natl. Acad. Sci. USA* **105**, 459–463 (2008).
- [30] Harris, T., Banigan, E., Christian, D. *et al.* Generalized Lévy walks and the role of chemokines in migration of effector cd8+ t cells. *Nature* **486**, 545–548 (2012).
- [31] Kumar, A. *et al.* Anomalous diffusion along metal/ceramic interfaces. *Nat. Commun.* **9**, 5251 (2018).
- [32] Ditlevsen, P. D. Observation of α -stable noise induced millennial climate changes from an ice-core record. *Geophys. Res. Lett.* **26**, 1441–1444 (1999).
- [33] Watkins, N. W. *et al.* The challenge of non-markovian energy balance models in climate. *Chaos* **34**, 072105 (2024).
- [34] Woringer, M., Izeddin, I., Favard, C. & Berry, H. Anomalous subdiffusion in living cells: Bridging the gap between experiments and realistic models through collaborative challenges. *Front. Phys.* **8**, 134 (2020).
- [35] Seckler, H., Szwabinski, J. & Metzler, R. Machine-learning solutions for the analysis of single-particle diffusion trajectories. *J. Phys. Chem. Lett.* **14**, 7910–7923 (2023).
- [36] Blümmler, P. & Soltner, H. Practical concepts for design, construction and application of Halbach magnets in magnetic resonance. *Appl. Magn. Reson.* **54**, 1701–1739 (2023).
- [37] Baun, O. & Blümmler, P. Permanent magnet system to guide superparamagnetic particles. *J. Magn. Magn. Mater.* **439**, 294–304 (2017).
- [38] Cranna, V. Karl pearson and sir ronald ross (2015). URL <https://blogs.lshtm.ac.uk/library/2015/03/27/karl-pearson-and-sir-ronald-ross/>. Library, Archive and Open Research Services blog.

- [39] Pearson, K. The problem of the random walk. *Nature* **72**, 294, 342 (1905).
- [40] Codling, E. A., Plank, M. J. & Benhamou, S. Random walk models in biology. *J. R. Soc. Interface* **5**, 813–834 (2008).
- [41] Lenz, F., Chechkin, A. V. & Klages, R. Constructing a stochastic model of bumblebee flights from experimental data. *PloS one* **8**, e59036 (2013).
- [42] Zaburdaev, V., Fouxon, I., Denisov, S. & Barkai, E. Superdiffusive dispersals impart the geometry of underlying random walks. *Phys. Rev. Lett.* **117**, 270601 (2016).
- [43] Volpe, G. & Volpe, G. The topography of the environment alters the optimal search strategy for active particles. *Proc. Natl. Acad. Sci. USA* **114**, 11350–11355 (2017).
- [44] Santana-Filho, J. V. *et al.* A Langevin dynamics approach to the distribution of animal move lengths. *J. Stat. Mech.: Theor. Exp.* **2020**, 023406 (2020).
- [45] Volpe, G., Gigan, S. & Volpe, G. Simulation of the active Brownian motion of a microswimmer. *Am. J. Phys.* **82**, 659–664 (2014).
- [46] Löwen, H. Inertial effects of self-propelled particles: From active Brownian to active Langevin motion. *The Journal of Chemical Physics* **152**, 040901 (2020).
- [47] Mandelbrot, B. B. & Van Ness, J. W. Fractional Brownian motions, fractional noises and applications. *SIAM Rev.* **10**, 422–437 (1968).
- [48] Jeon, J.-H. & Metzler, R. Fractional Brownian motion and motion governed by the fractional Langevin equation in confined geometries. *Phys. Rev. E* **81**, 021103 (2010).
- [49] Vitali, S. *et al.* Langevin equation in complex media and anomalous diffusion. *J. R. Soc. Interface* **15**, 20180282 (2018).
- [50] Bechinger, C. *et al.* Active particles in complex and crowded environments. *Rev. Mod. Phys.* **88**, 045006 (2016).
- [51] Sun, T. & Teja, A. S. Density, viscosity, and thermal conductivity of aqueous ethylene, diethylene, and triethylene glycol mixtures between 290 K and 450 K. *J. Chem. Eng. Data* **48**, 198–202 (2003).
- [52] Soltner, H. & Blümmler, P. Dipolar Halbach magnet stacks made from identically shaped permanent magnets for magnetic resonance. *Concepts Magn. Reson. Part A* **36**, 211–222 (2010).
- [53] Allan, D. B., Caswell, T., Keim, N. C., van der Wel, C. M. & Verweij, R. W. *soft-matter/trackpy: v0.6.1* (2023).

- [54] Newman, M. E. Power laws, Pareto distributions and Zipf's law. *Contemp. Phys.* **46**, 323–351 (2005).
- [55] Davies, R. B. & Harte, D. S. Tests for Hurst effect. *Biometrika* **74**, 95–101 (1987).
- [56] Orfanidis, S. J. *Introduction to signal processing* (Prentice-Hall, Inc., USA, 1995).
- [57] Virtanen, P. *et al.* Scipy 1.0: fundamental algorithms for scientific computing in Python. *Nat. Methods* **17**, 261–272 (2020).
- [58] Pedregosa, F. *et al.* Scikit-learn: Machine learning in Python. *J. Mach. Learn. Res.* **12**, 2825–2830 (2011).
- [59] Benelli, R. & Weiss, M. From sub- to superdiffusion: fractional Brownian motion of membraneless organelles in early *C. elegans* embryos. *New J. Phys.* **23**, 063072 (2021).
- [60] Khadem, S. M. J., Klapp, S. H. L. & Klages, R. Search efficiency of discrete fractional brownian motion in a random distribution of targets. *Phys. Rev. Res.* **3**, 023169 (2021).

Supplementary Information

Stochastic processes in the comoving frame

Here, we provide the theoretical underpinning for our experiments. We first introduce the comoving frame and illustrate its use by a simple example. We then define equations for overdamped stochastic dynamics in it by implementing our experimental constraint of constant speed. Next, we lay out a protocol to define trajectories with constant speed in this reference frame compatible with fractional Brownian motion, which we refer to as *fractional Brownian walks*. Finally, we outline the specific implementation of this protocol for our experiments.

The comoving frame

Stochastic processes are typically defined in a fixed Cartesian frame, as this can simplify their theoretical analysis. In contrast, our experiments are better described by stochastic dynamics formulated in a comoving frame in two dimensions (Fig. 1). This is a coordinate frame attached to the center of mass of a moving particle, whose x -axis is aligned with the velocity vector \mathbf{v}_{n-1} at any time step t_{n-1} , and the associated y -axis is perpendicular to it.⁶¹ It is thus corotating with the change of direction of the moving particle, and, hence, includes both translational and rotational movements. In this Cartesian comoving frame the velocity \mathbf{v}_n at the next time step t_n can be expressed in terms of its abscissa $v_{x,n}$ along the x -axis and its ordinate $v_{y,n}$ along the y -axis. However, it is more convenient to formulate the velocity \mathbf{v}_n at the next time step t_n in the comoving frame by its polar coordinates, speed v_n and turning angle φ_n (Fig. 1b). The pair (φ_n, v_n) at time steps t_n yields the coordinates of a particle in the comoving frame, and the corresponding time series fully determines its dynamics.

Because of our experimental constant speed constraint, we can directly consider overdamped dynamics in the form of correlated random walks.⁴⁰ These are defined by the time-discrete equations of motion in the comoving frame (Eqs. 1 and 2 in the main text):

$$\varphi_n = \xi_{\varphi,n} \tag{S1}$$

$$v_n = \xi_{v,n} . \tag{S2}$$

The terms $\xi_{\varphi,n}$ and $\xi_{v,n}$ represent two noises driving our experimental dynamics in this coordinate frame. In principle, these noises can be arbitrarily complex: they can depend on discrete time t_n ; they can also be coupled by featuring prefactors that may depend on both state variables; furthermore, they may be correlated in time.

Random walks

To illustrate this general framework, we can consider the two-dimensional time-discrete random walk put forward by Ross and Pearson about a century ago (Fig. 1, $\mu = 1$).^{38,39,62} If defined in a Cartesian coordinate frame, we can sample the two velocities, v_x and v_y , along x and y as independently and identically distributed random variables from two corresponding probability distributions, $\xi_{v_x,n} \sim \rho(v_x)$ and

$\xi_{v_y,n} \sim \rho(v_y)$, where here both distributions are symmetric Gaussians. Transforming these two velocities into polar coordinates of velocity orientation θ and speed v by using conservation of probability,⁶³

$$\rho(v_x)\rho(v_y)dv_xdv_y = \rho(\theta)\rho(v)d\theta dv, \quad (\text{S3})$$

yields a uniform distribution on the circle, $\rho(\theta) = (2\pi)^{-1}$, for the corresponding probability density of the orientation and a Rayleigh (two-dimensional Maxwell-Boltzmann) distribution for the corresponding probability density of the speed,

$$\rho(v) = \frac{v}{\sigma_v^2} e^{-\frac{v^2}{2\sigma_v^2}}. \quad (\text{S4})$$

where σ_v is the scale parameter of the distribution. After further wrapping on the circle and due to Markovianity, $\rho(\theta)$ delivers an equally uniform turning angle distribution $\rho(\varphi) = (2\pi)^{-1}$ (Fig. S5a). Sampling independent and identically distributed random variables from these turning angle and speed distributions according to Eqs. S1 and S2 by converting speeds into step lengths per time interval defines a time-discrete two-dimensional Ross-Pearson random walk in the comoving frame. Alternatively, one could sample the speeds from a (half-)Gaussian, as often done in the literature^{41,44} and in our experiments (Figs. 2 and S5), which due to the central limit theorem also yields Gaussian position distributions in the long-time limit, like the Ross-Pearson random walk.

Constant speed dynamics

In our experiments, a particle moves with a speed that is constant on average, and we can control the flight time τ_n during which it moves ballistically in the same direction (Fig. 1). Given some stochastic dynamics with variable speed v_n defined by Eqs. S1 and S2, our goal is to construct a corresponding stochastic process with constant speed that, for clarity of notation, here we denote as $v_c = \text{const.}$, which exactly preserves the topology of the paths generated by the original variable speed process. That is, a particle is supposed to move with constant speed on exactly the same paths generated by exactly the same step-length distribution for both dynamics. This implies that, instead of using constant flight times $\tau_n = \tau_c = \text{const.}$ for the variable speed dynamics, we use variable flight times τ_n for the constant speed dynamics by preserving the corresponding step lengths ℓ_n for both processes. Using the very same step lengths ℓ_n provides the crucial link between both dynamics. To do so, we need to transform Eq. S2 such that we can sample independently and identically distributed random variables from a distribution of flight times $\xi_{\tau,n} \sim \rho(\tau)$ instead of a speed distribution $\xi_{v,n} \sim \rho(v)$ (Eq. 3 in the main text).

We can perform this transformation as follows. Consider a stochastic process for the speed $v_n = \xi_{v,n}$, where the random variable $\xi_{v,n}$ is drawn independently and identically distributed from a given speed distribution $\rho(v)$, $\xi_{v,n} \sim \rho(v)$. Then the

distance ℓ_n traveled during a constant flight time τ_c is given by

$$\ell_n = v_n \tau_c. \quad (\text{S5})$$

This defines $\ell_n = \xi_{\ell,n}$ as a new, transformed random variable for which we need to calculate the associated step length distribution $\xi_{\ell,n} \sim \rho(\ell)$. This can be done again by conservation of probability (cf. Eq. S3), $\rho(v)dv = \rho(\ell)d\ell$, where the Jacobian is calculated from Eq. S5 yielding

$$\rho(\ell) = \frac{1}{\tau_c} \rho(v). \quad (\text{S6})$$

This completes the transformation from $v_n = \xi_{v,n} \sim \rho(v)$ to the associated stochastic process $\ell_n = \xi_{\ell,n} \sim \rho(\ell)$ at constant flight times τ_c .

Now assume that $v_n = v_c = \text{const.}$ instead of $\tau_n = \tau_c = \text{const.}$, as in our experiments (Fig. 1 and S2). We wish to preserve the step length ℓ_n at a given discrete time step n , as calculated above, so that the overall topology of a random path is preserved. That is, a particle traverses the very same distance ℓ_n for the very same turning angle φ_n at a time step n at now constant speed v_c , paying the price that it will now do so at a typically different (longer or shorter) associated variable flight time τ_n , making up for the corresponding original variable speed v_n . This is exactly the same idea underlying the transformation between Lévy flights and Lévy walks,^{3,6} which we implement here within the comoving frame. Accordingly, we now remove the assumption that $\tau_n = \tau_c = \text{const.}$ in Eq. S5, allowing again for variable flight times τ_n , by implementing instead the constant speed constraint $v_n = v_c = \text{const.}$ This leads to the complementary equation

$$\tau_n = \frac{\ell_n}{v_c}, \quad (\text{S7})$$

for the very same ℓ_n as above, where $\tau_n = \xi_{\tau,n}$ is sampled from a flight time distribution $\xi_{\tau,n} \sim \rho(\tau)$. The latter we can obtain from the step length distribution $\rho(\ell)$, Eq. S6, again by conservation of probability. Calculating the involved Jacobian by using Eq. S7 gives

$$\rho(\tau) = v_c \rho(\ell). \quad (\text{S8})$$

Feeding Eq. S6 into Eq. S8 yields the desired transformation between a given speed distribution at constant flight time τ_c and the corresponding flight time distribution at constant speed v_c ,

$$\rho(\tau) = \frac{v_c}{\tau_c} \rho(v). \quad (\text{S9})$$

The step lengths ℓ_n corresponding to flight times τ_n at constant speed v_c can be obtained from Eq. S7 yielding

$$\ell_n = v_c \xi_{\tau,n}, \quad (\text{S10})$$

which gives Eq. 3 in the main text.

As an example of applying this transformation scheme from variable speed at constant flight times to constant speed at variable flight times, consider the Rayleigh distribution for the speed mentioned at the end of the previous section. We wish to transform this distribution into a corresponding flight time distribution by assuming

now a constant speed v_c . We can do so by solving Eq. S5 for v_n , solving Eq. S7 for ℓ_n , and replacing ℓ_n in the former equation by the latter yielding

$$v_n = \frac{v_c}{\tau_c} \tau_n . \quad (\text{S11})$$

Applying this change of variables to the stationary Rayleigh speed distribution Eq. S4 yields for the associated stationary flight time distribution at constant speed

$$\rho(\tau) = \frac{\tau}{\sigma_\tau^2} e^{-\frac{\tau^2}{2\sigma_\tau^2}} , \quad (\text{S12})$$

with scale parameter $\sigma_\tau = \tau_c \sigma_v / v_c$, which is also a Rayleigh distribution. An α -stable Lévy speed distribution can be transformed into a corresponding α -stable Lévy flight time distribution exactly along the same lines. Since an exact definition for all parameter values $\alpha = 3 - \mu$ can only be given through its characteristic function in Fourier space, here we focus on the asymptotic representation in the form of power-law tails,^{3,6}

$$\rho(v) \approx C_1(\alpha) v^{-(\alpha+1)} (v \rightarrow \infty) \quad (\text{S13})$$

with $C_1(\alpha) = (1/\pi) \sin(\pi\alpha/2) \Gamma(1 + \alpha)$. Applying Eq. S11 then gives

$$\rho(\tau) \approx C_1(\alpha) \frac{v_c}{\tau_c} \tau^{-(\alpha+1)} (\tau \rightarrow \infty) , \quad (\text{S14})$$

yielding the functional form of Eq. 9, which was used for the experiments.

We emphasize that, while this general transformation between variable and constant speed is designed to preserve the topology of a given random path by preserving the step length generated at any discrete time step, it strictly yields a pair of variable- and constant-speed stochastic processes that are *not equivalent* to each other, see Eqs. 1 and 2 and Eqs. 1 and 3 in the main text. Clearly, for the former the speed distribution is not a δ -function while for the latter, by definition, it is, and vice versa for the corresponding flight time distributions. This non-trivial connection and its consequences for the corresponding stochastic properties have been amply explored in the literature, e.g., for Lévy flights and walks.^{3,6}

Finally, choosing for $\xi_{\varphi,n} \sim \rho(\varphi)$ in Eq. 1 a uniform distribution and for $\xi_{\tau,n} \sim \rho(\tau)$ in Eq. 3 a half-Gaussian distribution yields normal diffusion, while choosing for $\xi_{\varphi,n} \sim \rho(\varphi)$ in Eq. 1 a uniform distribution and for $\xi_{\tau,n} \sim \rho(\tau)$ in Eq. 3 an α -stable Lévy distribution defines a uniform Lévy walk in the comoving frame (Figs. 1, 2 and 3).⁴²

Fractional Brownian motion and walks

The previous transformation between variable-speed and constant-speed dynamics applies to Markovian stochastic processes, i.e. without memory between different steps ℓ_n . In our experiments, we also want to generate spatiotemporally correlated dynamics. A paradigmatic example of such a process is fractional Brownian motion (FBM). Therefore, in this section, we first discuss how to generate an analogue of

two-dimensional FBM in a comoving frame under the constraint of constant speed to then explain our specific experimental implementation (Fig. 4) in the following section (*Experimental implementation of fractional Brownian walks*). FBM is a Gaussian power-law correlated stochastic process that generates the whole spectrum of anomalous diffusion under parameter variation, from subdiffusion to superdiffusion through normal diffusion.^{47,60} While Lévy walks yield superdiffusion due to sampling the step lengths ℓ_n from power-law distributions instead of Gaussians (Figs. 1 and 2), FBM defines a fundamentally different class of anomalous stochastic process, where anomalous diffusion is due to a non-Markovian, power-law correlation decay of the velocity autocorrelation function (VACF) while sampling the velocities from Gaussian distributions.^{13,64}

FBM is a continuous process in space and time, which can be defined in terms of overdamped Langevin dynamics driven by fractional Gaussian noise (FGN).^{48,60} In one dimension, the corresponding equation reads

$$\frac{dx}{dt} = \xi_{\text{FGN}}(t), \quad (\text{S15})$$

where $\xi_{\text{FGN}}(t)$ holds for fractional, i.e. power-law correlated Gaussian noise^{48,60}

$$\langle \xi_{\text{FGN}}(t_1) \xi_{\text{FGN}}(t_2) \rangle = 2K_H H \left[(2H-1)|t_1 - t_2|^{2H-2} + 2|t_1 - t_2|^{2H-1} \delta(t_1 - t_2) \right] \quad (\text{S16})$$

with Hurst exponent $0 < H < 1$ and generalised diffusion coefficient K_H . The correlation function of the noise is thus identical with the VACF of the FBM process, which decays as a power law in time. From this equation, the mean squared displacement of FBM can be calculated to^{48,60}

$$\langle x^2(t) \rangle = 2K_H t^{2H}. \quad (\text{S17})$$

Under variation of the power-law exponent $\mu = 2H$, FBM displays the whole spectrum of anomalous diffusion.

For our experiments, we need to define a process at constant speed in the comoving frame that preserves the topology of the paths generated by FBM. Since, to our knowledge, no definition of such a stochastic process exists in this frame, we design a protocol to perform the required transformation. In line with our experimental setup, we define this protocol in terms of time- and space-discrete FBM.^{60,65} The crucial aspect for this transformation is to capture the non-Markovian correlations in Eq. S16 inherent to FBM. To do so, we consider a whole time series of a time-discrete FBM path (e.g. as generated in simulations) by recording the exact sequence of speeds and associated turning angles (v_n, φ_n) . We then use our change of variables in Eq. S11 to generate a Cartesian constant-speed version of FBM, defining the corresponding sequence of flight times and associated turning angles (τ_n, φ_n) . In addition to preserving the step lengths at any time step n , reproducing the velocity correlations requires us to also preserve the turning angles between pairs of velocities at subsequent n . Using the resulting full sequence of flight times and turning angles (τ_n, φ_n) at constant speed indeed enables us both to maintain the initial correlation (as we show below) and to

reproduce the topology of the original variable speed FBM in the comoving frame. We can consider this resulting constant-speed analogue of FBM as a *fractional Brownian walk*, in analogy to transforming Lévy flights into Lévy walks.⁶ The detailed protocol achieving this transformation from variable-speed to constant-speed FBM is defined as follows:

1. Generate two-dimensional time-discrete Cartesian FBM by a standard numerical algorithm.
2. Extract the sequence of speeds v_n and turning angles φ_n from a path of this numerically generated FBM at any time step $t_n = n\tau_c$ for given $\tau_c = \text{const}$.
3. For a given v_n in the sequence, calculate a corresponding flight time τ_n according to Eq. S11 by setting the desired speed $v_c = \text{const}$.
4. Reproduce the sequence of (τ_n, φ_n) pairs in the comoving frame with constant speed v_c , thus obtaining a constant-speed analogue of FBM in this frame that can be implemented with Eqs. 1 and 3.

The velocities of this process are no longer Gaussian-distributed nor are the speeds Rayleigh-distributed. However, according to Eq. S11, we can expect the flight-time distribution of this process at constant speed (corresponding to a variable-speed Gaussian stochastic process like FBM at constant flight times) to be Rayleigh-distributed (Eq. S12), as confirmed experimentally (Fig. S10). Most importantly, we expect this FBM-like process to still preserve the non-Markovian VACF decay (Eq. S16) as a defining feature of the original Gaussian FBM process. The latter property can be verified by starting from the definition of the VACF for an arbitrary non-constant speed, two-dimensional time-discrete process, given by

$$\langle \mathbf{v}_0 \mathbf{v}_n \rangle = \langle v_0 v_n \cos \varphi_n \rangle, \quad (\text{S18})$$

where, for $\mathbf{v}_0 \parallel x$, the angle φ_n is the polar angle between the velocity vector \mathbf{v}_0 at time step $n = 0$ and the velocity vector \mathbf{v}_n at time step n , with the angular brackets defining a suitable (time or ensemble) average. Assuming that the initial speed $v_0 = \text{const.}$, we can rewrite

$$\langle \mathbf{v}_0 \mathbf{v}_n \rangle = v_0 \langle v_n \cos \varphi_n \rangle. \quad (\text{S19})$$

As the polar coordinates, speed v_n and orientation φ_n , for the velocity vector \mathbf{v}_n are decoupled,

$$\langle \mathbf{v}_0 \mathbf{v}_n \rangle = v_0 \langle v_n \rangle \langle \cos \varphi_n \rangle. \quad (\text{S20})$$

Because, by definition, our protocol preserves all angles φ_n of the original time-discrete FBM process, we conclude that the VACF of the underlying original FBM process we started from is preserved if the constant speed $v_c = v_0$ fulfills the equation

$$v_c = \langle v_n \rangle. \quad (\text{S21})$$

For the speed-constant process, by averaging over Eq. S11 and using Eq. S21 we furthermore obtain

$$\tau_c = \langle \tau_n \rangle. \quad (\text{S22})$$

This relationship provides an important matching of timescales, indicating that the decay of the original FBM VACF can only be observed at times longer than the cutoff time defined by τ_c .

Experimental implementation of fractional Brownian walks

In our protocol above, we first need to generate FBM via a standard numerical algorithm, e.g. via the Davies-Harte method as done in our case.⁵⁵ However, the associated discretization of FBM⁶⁵ generates spurious dependencies on the Hurst exponent H , which propagate into this method.⁵⁵ To avoid introducing such dependencies, we initially simulated space-time-discrete FBM via the Davies-Harte algorithm setting the constant flight time ($\tilde{\tau}_c$) and the scale parameter ($\sigma_{\tilde{v}}$) to unitary values instead of directly setting the values needed for our experiments. Note that we now denote all variables generated in simulations with a tilde while all experimentally reproduced ones are still written without it. To match our experimental length scales, we then rescaled the distance $\tilde{\ell}_n$ traveled in simulations during the constant flight time $\tilde{\tau}_c$ by a factor κ , thus giving the actual experimental step length ℓ_n for our particles as

$$\ell_n = \kappa \tilde{\ell}_n. \quad (\text{S23})$$

We can therefore redefine all the relevant quantities discussed in the previous sections by taking this scaling into account. For brevity, in the following we just give the main results. After rescaling, Eq. S5 yields

$$v_n = \frac{\kappa \tilde{\ell}_n}{\tilde{\tau}_c} \quad (\text{S24})$$

with scaled speed

$$v_n = \kappa \tilde{v}_n. \quad (\text{S25})$$

Applied to Eq. S4, we obtain the scaled stationary Rayleigh speed distribution

$$\rho(v) = \frac{v}{\sigma_v^2} e^{-\frac{v^2}{2\sigma_v^2}} \quad (\text{S26})$$

with scale parameter $\sigma_v = \kappa \sigma_{\tilde{v}}$. Next, the scaled Eq. S7 reads

$$\tau_n = \frac{\kappa \tilde{\ell}_n}{\tilde{v}_c} \quad (\text{S27})$$

with scaled flight time

$$\tau_n = \kappa \tilde{\tau}_n. \quad (\text{S28})$$

Combining Eqs. S24 and S27 leads to the scaled change of variables

$$v_n = \frac{\tilde{v}_c}{\tilde{\tau}_c} \tau_n. \quad (\text{S29})$$

With this, we obtain the scaled Rayleigh flight time distribution

$$\rho(\tau) = \frac{\tau}{\sigma_\tau^2} e^{-\frac{\tau^2}{2\sigma_\tau^2}}, \quad (\text{S30})$$

with scale parameter $\sigma_\tau = \tilde{\tau}_c \sigma_v / \tilde{v}_c = \kappa \sigma_{\tilde{\tau}}$. Note that this distribution is defined with respect to the original parameters $\tilde{\tau}_c$ and \tilde{v}_c used in the simulations before scaling. Along the same lines, the scaled VACF is now given by

$$\langle \mathbf{v}_0 \mathbf{v}_n \rangle = \kappa^2 \langle \tilde{\mathbf{v}}_0 \tilde{\mathbf{v}}_n \rangle. \quad (\text{S31})$$

Following the same reasoning as before, we choose

$$v_c = \kappa \tilde{v}_c = \kappa \tilde{v}_0 \quad (\text{S32})$$

yielding, as a condition for the scaled constant-speed FBM dynamics to preserve the topology of the original FBM process,

$$v_c = \kappa \langle \tilde{v}_n \rangle = \langle v_n \rangle \quad (\text{S33})$$

as the scaled analogue to Eq. S21. Likewise, for the relevant timescale of the scaled constant-speed process, we obtain

$$\tau_c = \kappa \tilde{\tau}_c = \kappa \langle \tilde{\tau}_n \rangle = \langle \tau_n \rangle \quad (\text{S34})$$

as the scaled analogue to Eq. S22. As before, Eq. S34 provides an important matching of timescales, indicating that the decay of the original FBM VACF can only be observed at times longer than the scaled cutoff time defined by $\kappa \tilde{\tau}_c$. In our experiments, for sampling times δt below this cut-off time, one can indeed observe the typical exponentially decaying short-time correlation due to the particle's persistence in the magnetic driving field.⁴⁶

Supplementary figures

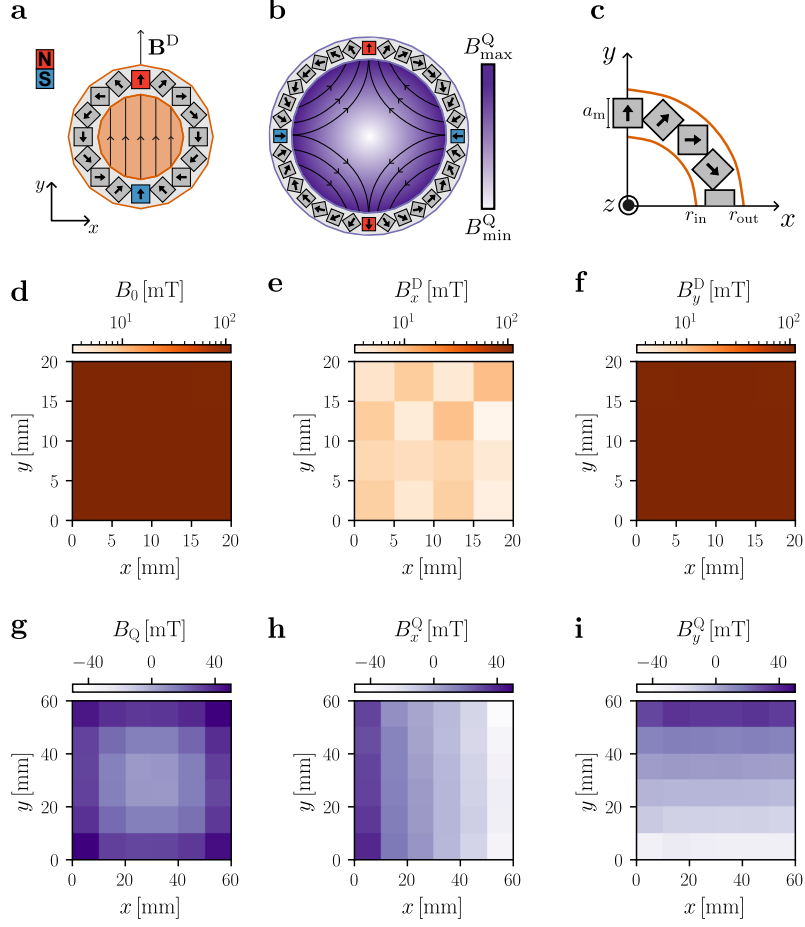


Fig. S1 Magnetic fields of the Halbach cylinders. (a-b) Schematics (in scale) of (a) a cylindrical Halbach dipole and (b) a cylindrical Halbach quadrupole. Both are built with permanent magnets (gray squares with black thick arrows pointing to the north poles of each magnet). The cylinders' magnetic north (red) and south (blue) as well as the flux lines are also shown. The strong dipolar field $\mathbf{B}^D = B_0 \mathbf{e}_y$ is homogeneous and directed along the y -axis of unit vector \mathbf{e}_y . The weaker quadrupolar field \mathbf{B}^Q consists of two orthogonal linear components. (c) Both configurations are composed of cubic magnets with side length a_m , arranged in a circular pattern in the xy plane with average radius r_c , inner radius r_{in} and outer radius r_{out} (Methods, Table 1). The inner radius r_{in} extends from the center of the cylinder to the inner edge of the magnets, defining the experimental area. The outer radius r_{out} , measured from the center of the cylinder to the outermost edge of the magnets, delimits the size of the cylinder. The axis of the cylinder is along the z -axis. (d) Measured magnetic field constant intensity B_0 of the Halbach dipole with its (e) x - and (f) y -components, B_x^D and B_y^D . B_x^D is one order of magnitude smaller than B_y^D . (g) Measured magnetic field intensity B_Q of the Halbach quadrupole with its (h) x - and (i) y -components, B_x^Q and B_y^Q . The two components are orthogonal and linear in space.

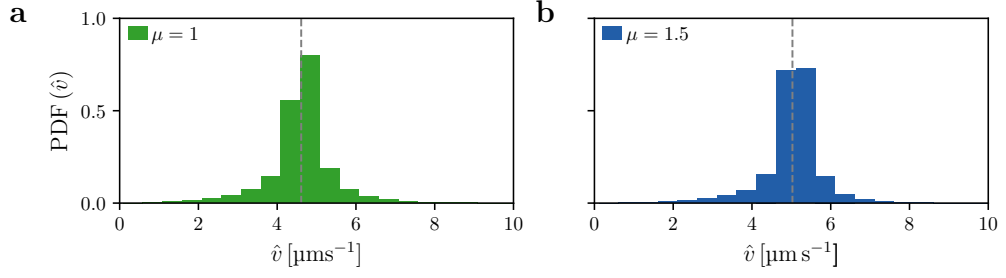


Fig. S2 Instantaneous particle's speed. (a-b) Probability density functions (PDF) of the instantaneous particle's speed \hat{v} extracted from the two trajectories in Fig. 1e for the cases of (a) normal diffusion ($\mu = 1$) and (b) superdiffusion ($\mu = 1.5$). The speed was calculated using a time window of 0.42 s (corresponding to five video frames) moving along the trajectory to minimize the impact of the particle's localization noise. The average speed (dashed vertical lines) is (a) $\langle \hat{v} \rangle = 4.61 \pm 0.82 \mu\text{m s}^{-1}$ and (b) $\langle \hat{v} \rangle = 5.03 \pm 0.74 \mu\text{m s}^{-1}$. Due to the narrow distributions, we consider the particles to move approximately at constant speed in our experiments.

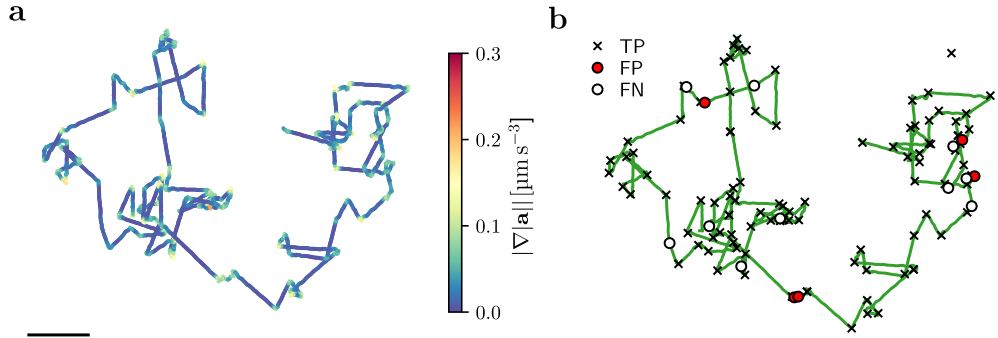


Fig. S3 Detection of turning points on particles' trajectories. (a) Portion of the normal diffusion trajectory in Fig. 1e with the absolute values of the acceleration magnitude gradient ($|\nabla|\mathbf{a}||$) overimposed. Peaks in this quantity identify the turning points (Methods). (b) The detected turning points are validated against the quadrupole rotations by calculating the F1 score from true positives (crosses, TP), false positives (filled circles, FP), and false negatives (empty circles, FN) (Methods). Scale bar: 25 μm .

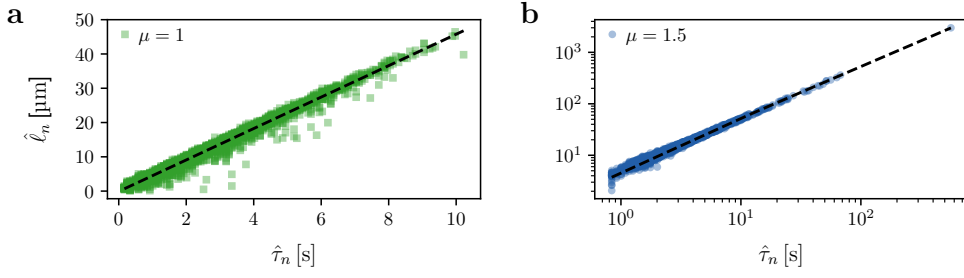


Fig. S4 Linearity between step lengths and flight times. Particle's step lengths $\hat{\ell}_n$ as a function of flight times $\hat{\tau}_n$ between turns extracted from the two trajectories in Fig. 1e for the cases of (a) normal diffusion ($\mu = 1$) and (b) superdiffusion ($\mu = 1.5$). The linear fits to the data (black dashed lines) confirms that the particles move at an approximately constant speed for all step lengths. The slope of the fit lines provides an estimate of the average speed of the particles alternative to the instantaneous velocity (Fig. S2): (a) $\langle \hat{v} \rangle = 4.585 \pm 0.009 \mu\text{m s}^{-1}$ and (b) $\langle \hat{v} \rangle = 5.298 \pm 0.002 \mu\text{m s}^{-1}$. These values are in good agreement with those in Fig. S2.

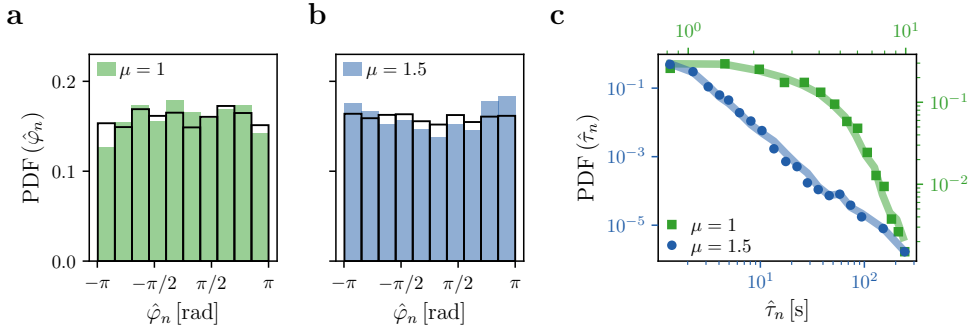


Fig. S5 Distributions of particles' turning angles and flight times. (a-b) Probability density functions (PDF) of the turning angles $\hat{\varphi}_n$ extracted from the two trajectories in Fig. 1e for (a) normal diffusion ($\mu = 1$) and (b) superdiffusion ($\mu = 1.5$). The PDFs of twice the quadrupole rotation angles ($\varphi_n = 2\Delta\beta$) are represented with black histograms in a-b, indicating uniform distributions on the circle and that $\text{PDF}(\hat{\varphi}_n) \sim \text{PDF}(\varphi_n) = \text{PDF}(2\Delta\beta)$ (Methods). (c) PDFs of particle's flight times $\hat{\tau}_n$ (as in Fig. 2a) for the two trajectories in Fig. 1e corresponding to normal diffusion ($\mu = 1$, green squares) and superdiffusion ($\mu = 1.5$, blue circles). The thick background lines are the PDFs of the quadrupole rotation times τ_n , showing that $\text{PDF}(\hat{\tau}_n) \sim \text{PDF}(\tau_n)$. The axis colors reflect those of the respective distributions.

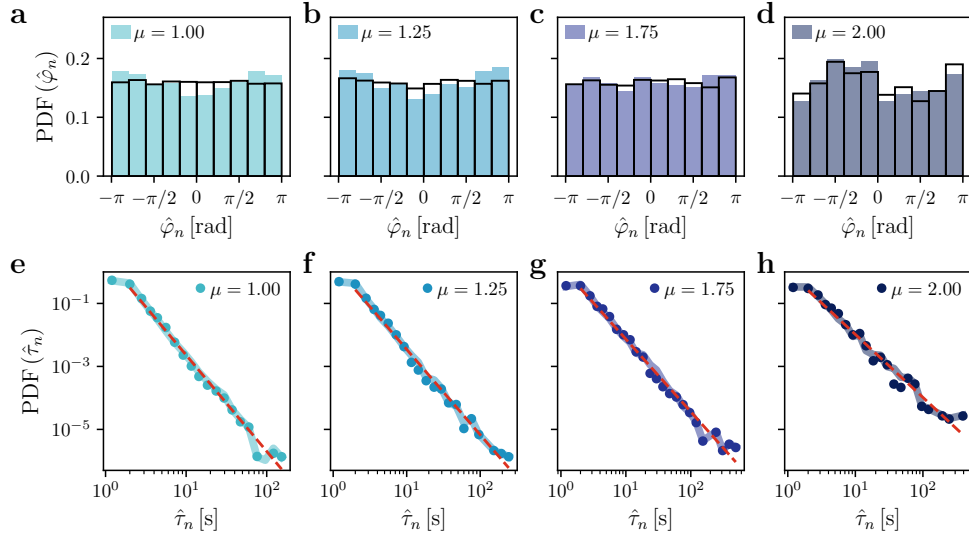


Fig. S6 Distributions of particles' turning angles and flight times for Lévy walks. Probability density functions (PDF) of (a-d) turning angles $\hat{\varphi}_n$ and (e-h) particle's flight times $\hat{\tau}_n$ for the trajectories in Fig. 3a, yielding Lévy walks with different anomalous diffusion exponents μ . In a-d, the PDFs of twice the quadrupole rotation angles ($\varphi_n = 2\Delta\beta$) are represented with black histograms, indicating uniform distributions on the circle and that $\text{PDF}(\hat{\varphi}_n) \sim \text{PDF}(\varphi_n) = \text{PDF}(2\Delta\beta)$ (Methods). In e-h, the data are fitted to power laws (red dashed lines) showing consistent scaling ($\sim \hat{\tau}_n^{\mu-4}$) with Lévy walk models (Table 2). The thick background lines are the PDFs of the quadrupole rotation time τ_n , showing that $\text{PDF}(\hat{\tau}_n) \sim \text{PDF}(\tau_n)$.

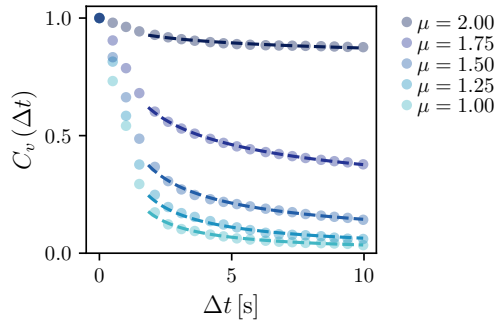


Fig. S7 Velocity autocorrelation function for Lévy walks. Normalised time-averaged velocity autocorrelation C_v as a function of lag time Δt for the trajectories in Fig. 3a, yielding Lévy walks with different anomalous diffusion exponents μ . Fitting the tail of the data with a power law (dashed lines) confirms the scaling characteristic of Lévy walks ($\sim \Delta t^{\mu-2}$, Table 2).

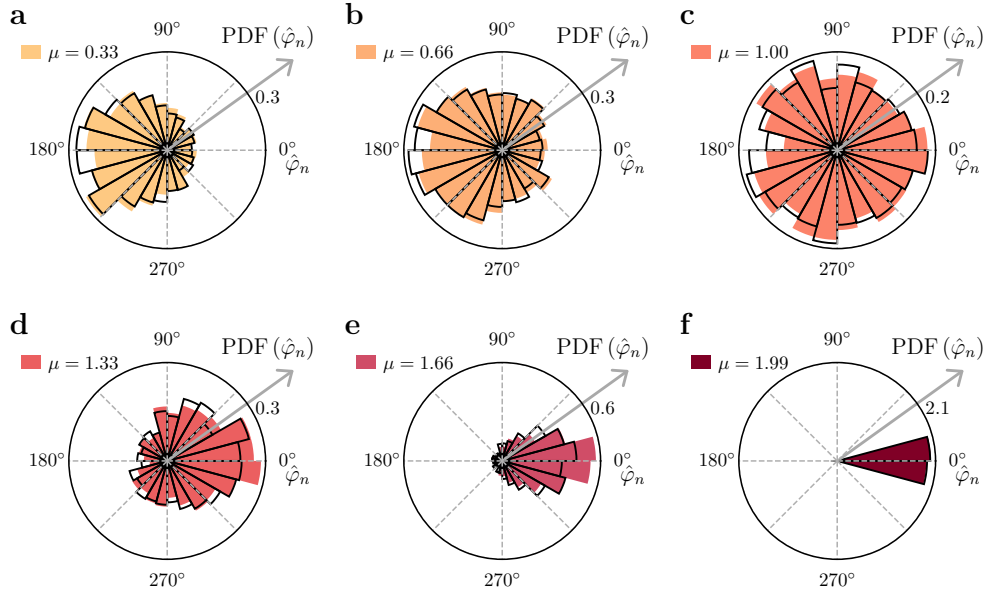


Fig. S8 Distributions of turning angles for fractional Brownian walks. Polar histograms of the particles turning angles $\hat{\varphi}_n$ from the trajectories in Fig. 4a showing the shift from backward (negative persistence) to forward propagation (positive persistence) as the anomalous diffusion exponent μ increases from subdiffusion (a: $\mu = 0.33$; b: $\mu = 0.66$) to diffusion (c: $\mu = 1$) to superdiffusion (d: $\mu = 1.33$; e: $\mu = 1.66$; f: $\mu = 1.99$). (a-b) In subdiffusive motion ($\mu < 1$), particles tend to move in a direction opposite to their previous one (towards 180°). This tendency is stronger the lower the values of μ . (c) For normal diffusion ($\mu = 1$), the uniform distribution of turning angles highlights the absence of directional correlations. (d-f) In superdiffusive regimes ($\mu > 1$), the particle is likely to maintain their current direction (towards 0°), as in directed motion. This tendency is stronger the higher the values of μ . The black solid lines represent the distributions of twice the quadrupole rotation angle for reference.

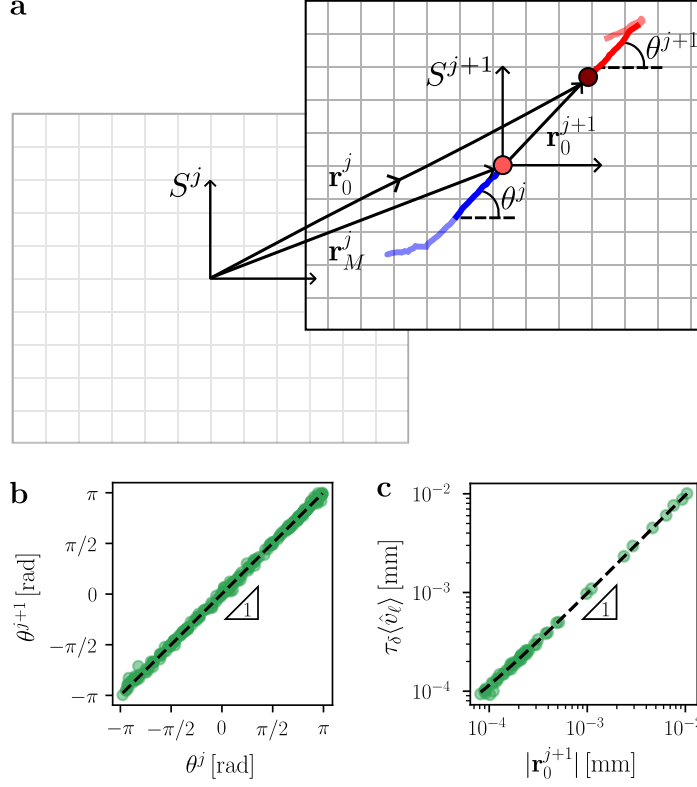


Fig. S9 Trajectory stitching. (a) Vectorial relationship (Eq. 7) for the translation of the trajectory points \mathbf{r}_i^{j+1} (red) acquired in the coordinate systems S^{j+1} of the $(j+1)^{\text{th}}$ video back to points \mathbf{r}_i^j (blue) in the coordinate system S^j of the j^{th} video to reconnect them to the previous part of the full particle's trajectory. \mathbf{r}_M^j is the position of the last recorded point in the j^{th} video in its reference system, and \mathbf{r}_0^{j+1} and \mathbf{r}_0^j respectively identify the first particle's position in the $(j+1)^{\text{th}}$ video in its reference system and in the reference system of the j^{th} video. To facilitate interpolation of the stitched trajectory, any two consecutive videos respectively finished (dark blue line) and started (dark red line) with an at least 1-s long portion of the same step length in the full trajectory, with polar angles θ^j and θ^{j+1} in each respective reference system. The side length of each grid square corresponds to $5 \mu\text{m}$. (b) Linear relationship between θ^j and θ^{j+1} showing that $\theta^{j+1} \approx \theta^j$. A linear fit to $f(\theta^j) = k'\theta^j$ (dashed line) with slope $k' = 1.002 \pm 0.002$ confirms that the direction of motion is preserved during the reconstruction of the trajectory. (c) Linear relationship between direct measurements of the distance $|\mathbf{r}_0^{j+1}|$ (from image analysis and measurements of stage displacement) and its estimate as $\tau_\delta \langle \hat{v}_\ell \rangle$, where $\langle \hat{v}_\ell \rangle$ is the mean particle's speed in the two reconnected portions from the same step length and τ_δ is the time elapsed between recordings of two consecutive videos. A linear fit to $f(|\mathbf{r}_0^{j+1}|) = k'|\mathbf{r}_0^{j+1}|$ with slope $k' = 0.965 \pm 0.003$ confirms the good match between these two values. Linear trend with slope 1 shown for reference in b-c.

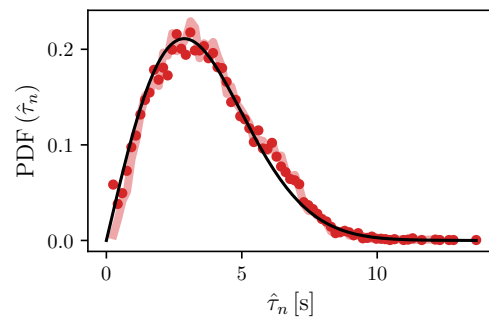


Fig. S10 Flight time distribution for fractional Brownian walks. Probability density function (PDF) of particles' flight times ($\hat{\tau}_n$) for all fractional Brownian walks (Fig 4a). Data collapse on a Rayleigh distribution given by Eq. S30 (black solid line), independent of the value of the anomalous diffusion exponent μ . The thick background line is the PDF of the quadrupole rotation time τ_n , showing that $\text{PDF}(\hat{\tau}_n) \sim \text{PDF}(\tau_n)$.

Supplementary tables

Table 1 Parameters of the Halbach cylinders. Remanence B_R and relative permeability μ_R of k cubic neodymium magnets with side length a_m used to build two identical circular arrays for the Halbach dipole and one for the Halbach quadrupole for the experiments. The Halbach cylinders are characterized by the following parameters: inner radius r_{in} , outer radius r_{out} , average radius r_c and height $h = a_m$.

Halbach cylinder	k	B_R [T]	μ_R	a_m [mm]	r_{in} [mm]	r_{out} [mm]	r_c [mm]	h [mm]
Dipole	16	1.48	1.05	9.5	23.3	36.8	30.05	9.5
Quadrupole	32	1.32	1.05	7	41.8	51.6	46.7	7

Table 2 Estimated anomalous diffusion exponent $\hat{\mu}$ for Lévy walks (Figs. 2 and 3) based on fitting the mean squared displacement ($\hat{\mu}_{\text{MSD}}$, Figs. 1 and 3), the quadrupole time probability distribution function ($\hat{\mu}_{\tau_n}$, Figs. 2, S5 and S6), the flight time probability distribution function ($\hat{\mu}_{\hat{\tau}_n}$, Figs. 2, S5 and S6), the step length probability distribution function ($\hat{\mu}_{\hat{\ell}_n}$, Figs. 2 and 3), and the velocity autocorrelation function ($\hat{\mu}_{C_v}$, Fig. S7). The first column shows the corresponding ground truth value of μ . Corresponding instantaneous particle's speed $\langle \hat{v} \rangle$ are also shown. Errors represent one standard deviation of the respective fit parameters.

μ	$\langle \hat{v} \rangle$ [$\mu\text{m s}^{-1}$]	$\hat{\mu}_{\text{MSD}}$	$\hat{\mu}_{\tau_n}$	$\hat{\mu}_{\hat{\tau}_n}$	$\hat{\mu}_{\hat{\ell}_n}$	$\hat{\mu}_{C_v}$
1.00	5.03 ± 0.97	1.0509 ± 0.0002	0.93 ± 0.09	0.94 ± 0.08	0.95 ± 0.06	1.039 ± 0.010
1.25	4.88 ± 0.95	1.2578 ± 0.0003	1.30 ± 0.05	1.29 ± 0.07	1.22 ± 0.07	1.200 ± 0.013
1.50	5.03 ± 0.74	1.5473 ± 0.0004	1.49 ± 0.04	1.46 ± 0.06	1.45 ± 0.05	1.434 ± 0.005
1.75	5.11 ± 0.75	1.7498 ± 0.0003	1.71 ± 0.06	1.70 ± 0.06	1.71 ± 0.09	1.704 ± 0.001
2.00	4.46 ± 0.93	1.9158 ± 0.0003	2.05 ± 0.06	2.00 ± 0.08	2.03 ± 0.07	1.964 ± 0.001

Table 3 Estimated anomalous diffusion exponent $\hat{\mu}$ for fractional Brownian walks (Fig. 4) based on fitting the mean squared displacement ($\hat{\mu}_{\text{MSD}}$) and the velocity autocorrelation function ($\hat{\mu}_{C_v}$). The first column shows the corresponding ground truth value of μ . Corresponding instantaneous particle's speed $\langle \hat{v} \rangle$ are also shown. Errors represent one standard deviation of the respective fit parameters.

μ	$\langle \hat{v} \rangle$ [$\mu\text{m s}^{-1}$]	$\hat{\mu}_{\text{MSD}}$	$\hat{\mu}_{C_v}$
0.33	3.92 ± 0.76	0.36944 ± 0.00030	0.29 ± 0.08
0.66	4.99 ± 0.84	0.67492 ± 0.00028	0.67 ± 0.09
1.00	5.66 ± 0.82	0.95485 ± 0.00022	1.00 ± 0.08
1.33	4.98 ± 0.78	1.29699 ± 0.00023	1.27 ± 0.06
1.66	4.60 ± 0.91	1.67541 ± 0.00021	1.60 ± 0.05
1.99	3.71 ± 0.56	1.98648 ± 0.00003	2.00 ± 0.06

Supplementary References

- [61] Romanczuk, P., Bär, M., Ebeling, W., Lindner, B. & Schimansky-Geier, L. Active brownian particles. *Eur. Phys. J. Spec. Top.* **202**, 1–162 (2012).
- [62] Pearson, K. Mathematical contributions to the theory of evolution - a mathematical theory of random migration. *Biometric Ser.* **3**, 54 (1906).
- [63] Gardiner, C. *Stochastic Methods: A Handbook for the Natural and Social Sciences*. Springer Series in Synergetics (Springer, Berlin, 2009).
- [64] Embrechts, P. *Selfsimilar processes* (Princeton University Press, Princeton, New Jersey, USA, 2009).
- [65] Molz, F. & Liu, H. Fractional brownian motion and fractional gaussian noise in subsurface hydrology: A review, presentation of fundamental properties, and extensions. *Water Res. Res.* **33**, 2273–2286 (1997).